UNIVERSITY OF CALIFORNIA,
IRVINE

Advanced Experimental Techniques for High Resolution Detection of Aft-Emitted Tonal Fan Noise

THESIS

submitted in partial satisfaction of the requirements
for the degree of

MASTER OF SCIENCE

in Mechanical and Aerospace Engineering

by

Kyle Miller

Thesis Committee:
Professor Dimitri Papamoschou, Chair
Professor Perry Johnson
Professor Feng Liu

2023

TABLE OF CONTENTS

LIST OF FIGURES

LIST OF TABLES

ACKNOWLEDGMENTS

I would first like to thank my advisor, Professor Dimitri Papamoschou for his support and mentorship. Much of my work would not have been possible without his guidance and wisdom. His work ethic and astuteness has guided me to becoming a better engineer and his passion has ignited my enthusiasm for the world of aeroacoustics.

I would also like to thank my partner Rae for her support during my education. She has brought me courage and motivation to continue with my work both on the good days and it is with her help that I am able to write this report with a smile on my face.

I want to thank my friends Christian, Chris and Collin as well as my family Todd, Margie and Taylor Miller for their dedication to my success. They have helped support me both mentally and financially throughout my life and without them by my side I would be nowhere near where I am now. I would also like to extend a special thanks to my grandmother Hinda Brush who worked alongside me to write her PhD dissertation as I was writing this document.

I am especially grateful to my committee Professor Dimitri Papamoschou, Professor Perry Johnson and Professor Feng Liu for their dedication to my work as well as the work put forth by the University.

I would like to thank a personal mentor of mine, David Morata, for guiding me as I wobbled into graduate school. Without his help our laboratory would most surely be on fire by now.

Lastly, I would like to acknowledge the support of the NASA Small Business Innovation and Research (SBIR) program as well as ATA for funding part of this work, from the funding contract number 80NSSC20C0089.

ABSTRACT OF THE THESIS

Advanced Experimental Techniques for High Resolution Detection of Aft-Emitted Tonal Fan Noise

By

Kyle Miller

Master of Science in Mechanical and Aerospace Engineering

University of California, Irvine, 2023

Professor Dimitri Papamoschou, Chair

The near acoustic field of a subscale ducted fan was experimentally measured for the purpose of understanding the physics of sound generation and refining low-order models for aft-emitted tonal fan noise. To properly resolve the detailed features of the pressure field, measurements were obtained using a phased microphone array comprising of fixed and scanning sensors. The traversing of a sensor through a spatially-varying acoustic field introduces signal non-stationarity which must be addressed by dividing the complete signal into quasi-stationary blocks and applying a frequency-dependent window during spectral estimation. The harmonic content of the pressure along the scan line was obtained from the signals of the axially scanning sensors using the Vold-Kalman (VK) filter and partial fields decomposition (PFD). Accurate construction of the axial pressure distribution from the microphone measurements required advanced interpolation and filtering techniques based on the the decomposition of the pressure into its unwrapped phase and amplitude. The resulting axial pressure field has sufficient spatial resolution to perform space-time correlations and calculate the convective Mach number distribution. The azimuthal distribution of the tonal pressure field was obtained from the fixed sensors using the VK filter and can be combined with the axial pressure distribution to generate a cylindrical radiation surface. The radiation surface can then be implemented into propagation and scattering tools, such as the bound-

ary element method (BEM), to efficiently predict acoustic emission in isolated and installed configurations. The near-field measurements are compared to the predictions of a model for aft tonal emission where the source features are partially informed by the internal duct acoustics. Reasonable agreement is found in the axial pressure distributions and space-time correlations. The near-field measurements can provide guidance for refinement of the model.

Nomenclature

a	=	ambient speed of sound
$\mathcal{D}$	=	decay function
D_e	=	fan exit diameter
$\mathbf{G}$	=	cross-spectral matrix
k_a	=	acoustic wavenumber
k_r	=	radial wavenumber in duct acoustics
k_x	=	axial wavenumber in duct acoustics
K	=	number of block divisions
m	=	azimuthal mode number
$\mathcal{M}$	=	number of microphones
M	=	duct Mach number
M_c	=	convective Mach number
n	=	radial mode number
n_{BPF}	=	blade passing frequency harmonic
$p_i(t)$	=	pressure signal of microphone i
$\hat{p}_i(\omega)$	=	Fourier transform of $p_i(t)$
P	=	phasor of pressure signal
r	=	radial coordinate
R	=	correlation coefficient
R_o	=	exit radius of fan nozzle
t	=	time
U	=	duct velocity
U_c	=	convective velocity
V_m	=	microphone speed
$\mathbf{U}, \mathbf{V}$	=	matrices used in singular value decomposition
x	=	axial coordinate
$\mathbf{z}, \mathbf{Z}$	=	parameter vectors
θ	=	polar angle
κ_r	=	radial wavenumber in outward propagation
κ_x	=	axial wavenumber in outward propagation
ξ	=	axial separation
$\mathbf{\Pi}$	=	partial fields vector
ϕ	=	azimuthal angle

Σ	=	singular value matrix
τ	=	time shift
ω	=	radian frequency
Ω	=	fan rotation rate
ψ	=	sensor phase

Subscripts

k	=	block index
F	=	fixed microphone
S	=	scanning microphone

Acronyms

BEM	=	Boundary Element Method
BPF	=	Blade Passing Frequency
CSD	=	Cross Spectral-Density
CSM	=	Cross-Spectral Matrix
FFT	=	Fast Fourier Transform
PFD	=	Partial Fields Decomposition
PSD	=	Power Spectral Density
VK	=	Vold-Kalman

Chapter 1

Introduction

1.1 Motivation

The St. Petersburg-Tampa Airboat Line was the first fixed-wing commercial airline and began operation January 1^{st}, 1914. The airline offered customers the chance to experience the fresh Florida air and a salty spray in their face as they took the 23-minute flight over Tampa bay. [2]. While the airline stopped service after only four months, the aviation industry continued to grow exponentially, reaching approximately 4.1 billion transported passengers in 2017 alone.[3]. With the growth of the aviation sector, noise emissions have become one of the most impactful adverse side effects of the industry and is linked with negative health effects including community annoyance, sleep disturbance, cardiovascular disease, and mental health problems [4]. Properly mitigating the impact of the aviation industry on community noise pollution requires a detailed understanding of how aircraft noise is generated and its interaction with the surroundings. The process of obtaining this information is known as noise source localization and has been a topic of intense research over the last eighty years [5].

Initial efforts at localizing aircraft noise sources began during World War II with the development of acoustic telescopes. [6]. These rudimentary setups consisted of parabolic mirrors that reflected the incoming acoustic waves to a singular focal point. The summation of the waves at the focal point generated signal measurements sufficiently larger than the measurement noise and allowed for the detection of approaching aircraft from far away. While the acoustic telescopes allowed for aircraft detection, their resolution was insufficient to give any indication to how the noise was generated.

After World War II, the National Advisory Committee for Aeronautics (NACA) began pushing for noise reduction of propeller driven aircraft. These efforts were initially undertaken in a series of experimental studies by Hubbard alongside various authors [7–9]. The experiments focused on measuring the effect of propeller geometry on the emitted acoustic field including the impact of tip Mach number, blade number and propeller rotation rate. While these studies were able to properly determined the effects of these parameters on the resulting acoustic field, a lack of sensor resolution continued to restrict their ability to precisely characterize the noise sources.

As the turbojet engine became more commonplace in commercial aviation, the demand for reducing aircraft noise increased. Turbojet noise emissions are dominated by fan and jet noise, the former containing strong emissions at discrete frequencies that can be more objectionable than the broadband exhaust noise. [10]. An analytical analysis of the fan noise at these discrete frequencies was performed by Sofrin in conjunction with various authors [10, 11]. Their analysis concluded that the tonal acoustic field generated by a rotating fan within a duct is given by a summation of modes determined by the duct geometry and fan operation conditions. Their result has been seminal to the study of tonal fan noise and is the foundation for internal duct acoustics. The analysis was expanded on by Munt [12] who analytically solved for the sound radiation emanating from a semi-infinite annular duct. Munt's analysis confirmed the existence of modes within the duct and suggested that the

shape of the tonal acoustic field predicted by internal duct acoustics is maintained within the shear layer outside the duct. [12].

Alongside the development of duct acoustic theory, significant efforts were invested into developing more sophisticated experimental setups. The introduction of the traditional phased microphone array provided unprecedented experimental resolution which allowed for more accurate characterization of acoustic sources. An initial effort that utilized these improvements is published by Fisher *et al.* [13]. The study utilized an experimental rig containing sensors distributed over a polar arc centered on the axis of a high-speed jet. Using cross-correlations and cross-spectral densities between distinct sensors the authors were able to disseminate the space-frequency distribution of the main jet noise sources. Their methodology proved so successful that it continues to be a basis for all modern noise source localization techniques. Despite the advancements made to experimental protocols, the resolution of the traditional phased array still remained insufficient to fully characterize the tonal acoustic field predicted by duct acoustics.

As the high-bypass turbofan engine began to replace the turbojet, fan noise emissions became more prominent in commercial aircraft. Meanwhile, modern advancements in computational power, allowed the original analytical analysis performed by Sofrin, Munt and others to be explored computationally. One of the most significant contributions was a series of investigations in which a computational model was developed based on the linearized Euler equations and was used to solve for the sound radiating from an axisymmetric duct on a 2D domain. [14–18]. The simulation results reflected the theoretical development of internal duct acoustics and coincide with Munt's prediction that the external acoustic field retains the characteristics of the internal field. Additionally, the computational results suggested that the directivity of the external acoustic field was reminiscent of Mach wave radiation measured in jets [18].

In conjunction to the computational investigations, advancements in experimental protocols

were made as the utilization of microphone arrays consisting of both fixed and continuously-scanning sensors gained interest. The use of scanning sensors enables a spatial resolution capable of resolving the fine details of the acoustic field and can be thought of as an extension to the start-and-stop method of Lee and Bolton [19]. Application of continuously scanning microphone arrays has been successfully implemented for high resolution detection of acoustic sources in both jet and fan noise [20, 21].

As the generation mechanisms of duct noise became better understood through combined analytical, computational and experimental studies, attempts for suppressing the noise emissions were investigated. Reduction techniques have centered around shielding the engine noise through clever integration of the engine with the airframe. The blended wing body (BWB) airframe design has been central to these efforts [22] however, the complexity of airframe integration requires that designers have the ability to inexpensively asses a multitude of possible airframe configurations. To aid in achieving this goal, efforts have been undertaken by Truong and later modified by Papamoschou [1, 23, 24] to generate a surface-based model for aft-emitted tonal fan noise. The surface-based model was inspired through previous efforts by Papamoschou in jet noise modeling [25–27] with the distinction being that tonal fan noise is deterministic.

The proposed surface based model is parameterized using far-field measurements [1] however, there currently exists no high-resolution near-field experimental measurements that can be used to verify that the model encapsulates the proper physics of noise generation. The goal of the present work is therefore to utilize advanced experimental techniques to characterize the tonal aft-emitted acoustic field emanating from a ducted fan for the purpose of understanding the physics of sound generation and refining low-order models.

1.2 Research Goals

The goal of the research presented is the application of advanced acoustic testing techniques to continuously-scanning sensors in an attempt to characterize the near-field aft-tonal emissions of a ducted fan. The acoustic field will be characterized by the axial and azimuthal pressure distributions. The resulting pressure distributions are used to determine the azimuthal order and convective Mach number distribution of each tone. These parameters are used to refine and verify a surface-based source model previously calibrated from far-field measurements. This project included the design of a near-field microphone array containing a fixed azimuthally-phased array in conjunction with a scanning axially-phased array. Guidelines for proper experimental procedures and microphone signal processing are included and a comparison between time and frequency domain processing is demonstrated. The remaining sections are organized as follows.

Chapter 2 provides an overview of the acoustic spectrum as a measurement of noise emissions in addition to the theoretical development for ducted fan noise which has been used to inform the source model and experimental procedure.

The advanced experimental techniques utilized in characterizing tonal fan noise during this investigation is presented in Chapter 3. The time and frequency domain processing are both presented and have an important impact on the quality of the resulting noise source characterization. The discussed signal processing techniques are also extended for cases where a subset of the used sensors are scanning a non-stationary acoustic field.

The experimental setup is discussed in Chapter 4. The details of the UCI anechoic chamber, near-field microphone array and small-scale ducted fan are all introduced. The data acquisition parameters are outlined and guidelines for selecting the optimal design setups are discussed. A brief overview of the performed experiments is provided.

Chapter 5 characterizes the 2^{nd} and 3^{rd} harmonic of the blade passing frequency through the convective Mach number and complex pressure along the scan line. The azimuthal order of each mode at the axial location of peak emission is also provided. The near-field measurements are then compared with the model predictions.

Chapter 6 provides a brief summary of the work and outlines future considerations.

Chapter 2

Background

This chapter introduces the concepts and equations that are central to the study of noise generation within a ducted fan. First, a brief overview on the behavior of acoustic waves is provided along with fundamental metrics used for the classification of noise source emissions. Next, a review on the fundamental components of aft-emitted tonal fan noise is provided. Finally, an introduction to a low-order source model originally proposed by Papamoschou and Truong [23] is presented.

2.1 The Nature of Acoustic Waves

For a given flow, the pressure field can be decomposed into a base mean and a fluctuating pressure. Neglecting viscosity, the fluctuating pressure is governed by the Euler equations and for a sufficiently small disturbance in a quiescent medium, the linearized governing equations dictate that the pressure fluctuation obeys the wave equation

$$\frac{\partial^2 p}{\partial t^2} - a^2 \nabla^2 p = 0 \tag{2.1}$$

where a is the ambient speed of sound and p is the pressure fluctuation.

Noise is perceived by the human body in terms of pitch and volume. The sound pitch is associated with the frequency of the sound pressure while the volume is associated with the acoustic power of the pressure. When measuring the noise emissions of a source, it therefore becomes of interest to determine how the sound's power is distributed across all emitted frequencies. This power distribution is called the power spectrum and is a common metric used when characterizing an acoustic source's emissions.

Given the importance of the frequency content, Fourier analysis plays a big role in the measurement of sound. It is based on the timewise Fourier transform of the pressure fluctuation $p(t)$:

$$\widehat{p}(\omega) \;=\; \int_{-\infty}^{\infty} p(t) e^{-i\omega t} dt \tag{2.2}$$

where ω is the radian frequency. For $p(t)$ random, $\widehat{p}(\omega)$ is also a random variable and thus of limited usefulness on its own. Strictly speaking, $\widehat{p}(\omega)$ may not even exist. This limitation is overcome by first defining a finite-time Fourier transform according to

$$\widehat{p}_T(\omega) \;=\; \int_{-T}^{T} p(t) e^{-i\omega t} dt \tag{2.3}$$

then performing the averaging of $\widehat{p}_T \widehat{p}_T^*$, where $*$ denotes the complex conjugate. This results in the approximate definition of the power spectral density

$$S(\omega) \;=\; \lim_{T\to\infty} \; \frac{1}{2T} \, \widehat{p}_T(\omega) \, \widehat{p}_T^*(\omega) \tag{2.4}$$

In practice, the power spectral density is evaluated by dividing the signal into segments and performing the operation $\widehat{p}_T \widehat{p}_T^*$ for each segment, often using the Fast Fourier Transform (FFT) algorithm. Then the result is averaged over all the segments.

For the rest of the thesis, the spectral averaging operation of Eq. (2.4) will be presented as

$$S(\omega) \;=\; \overline{\widehat{p}(\omega)\;\widehat{p}^{*}(\omega)} \tag{2.5}$$

and will be applied to power spectral densities as well as cross-spectral densities.

The exact definition of the power spectral density is the Fourier transform of the autocorrelation $< p(t)p^{*}(t+\tau) >$, where $< . >$ denotes the time average. However, this definition is impractical for numerical evaluation and the averaging of Eq. (2.5) is used instead.

The dynamic range of the PSD is typically large such that it becomes convenient to express it on a logarithmic scale. Additionally, it becomes useful to reference the measured sound pressure to a reference value. Throughout this investigation the reference pressure is chosen based on the minimum audible sound pressure to the human ear, $p_{ref} = 20\mu Pa$. After these modifications, the resulting measurement is the raw sound pressure level (SPL) spectrum and is measured in $[dB/Hz]$.

$$SPL(\omega) = 10\log_{10}\left(\frac{S(\omega)}{p_{ref}^{2}}\right) \tag{2.6}$$

The true SPL is obtained by correcting the raw SPL for atmospheric absorption, the microphone frequency response and the free-field response. A detailed description of these corrections are provided in Ref. [28]. The SPL spectrum is commonly used to asses the emissions of an acoustic source.

Generally, the PSD can be decomposed into the contributions from a broadband and a harmonic spectrum. The broadband spectrum is comprised of the spectral densities across a wide range of frequencies and is attributed to the random turbulent interactions within the flow. The tonal components occur at distinct frequencies and are associated with noise generation from cyclic processes. The tonal noise components often contain the largest

amplitudes within the power spectrum.

A harmonic source may not necessarily emit at a single frequency. Often, the emission is at multiple integers of the lowest frequency. The lowest frequency is the fundamental frequency and the integer multiples are the harmonics. When observing the power spectrum of a tonal noise source one will therefore notice significant contributions at both the fundamental frequency as well as the frequency of each harmonic. An example PSD for the aft-emission of a small-scale ducted fan is provided in Fig. 2.1. The first five harmonics of the fundamental tone are visible with the first two harmonics dominating the spectrum.

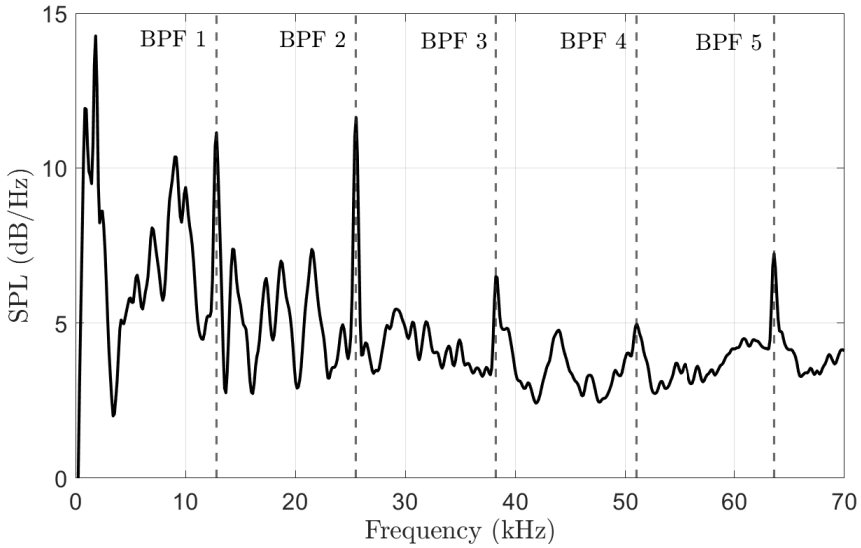

Figure 2.1: Power spectrum for aft-emissions of a small-scale ducted fan at a polar angle of θ=67.5°. Black dashed line indicates each harmonic of the fundamental.

2.2 Review of Tonal Fan Noise

Tonal fan noise is a result of the displacement of fluid volume caused by the passage of a fan blade through a point in space. The fluid displacement results in a fluctuation of the pressure field and for a continuously rotating fan, will periodically generate pressure perturbations. Should these perturbations continue to propagate away from the source,

they will be perceived by an observer as noise. The fundamental frequency at which these pressure disturbances are generated is denoted as the blade passing frequency (BPF) and is determined by the fan blade count B and rotation rate Ω. The resulting radian frequency is given by

$$\omega = \Omega B \tag{2.7}$$

The periodic pattern of the pressure disturbances is not exactly sinusoidal and recreating the pattern using a Fourier series therefore requires that we utilize sines and cosines not only at the fundamental frequency but at integer harmonics as well. The power spectrum of the fan emissions will therefore contain a series of contributing frequencies given by

$$\omega = n_{BPF}\Omega B \tag{2.8}$$

where $n_{BPF} = 1, 2, ..., n$ and represents the index of each harmonic. Each harmonic of the fundamental tone will be denoted by its integer multiple, with the 2^{nd} harmonic denoted as $n_{BPF} = 2$ and so on.

Considering now a fan placed within an annular duct containing uniform axial flow, the pressure disturbance in the duct will satisfy the convective wave equation [23]

$$\frac{1}{a^2}\left(\frac{\partial}{\partial t} + U\frac{\partial}{\partial x}\right)^2 p - \nabla^2 p = 0 \tag{2.9}$$

where x is the axial coordinate, U is the axial velocity and ∇^2 is the three-dimensional Laplace operator in cylindrical coordinates. The presence of the duct constrains that the radial velocity, and therefore the radial gradient of the sound pressure, is zero along the duct walls. For an annular duct this takes the form

$$\frac{\partial p}{\partial r} = 0 \quad ; \quad r = R_i, R_o \tag{2.10}$$

where R_i and R_o are the inner and outer duct radius respectively. The problem is now reduced to the cylindrical convective wave equation with linear homogeneous boundary conditions and can readily be solved using separation of variables. For a harmonic field, the resulting pressure perturbation takes the form

$$p = R(r)e^{i(k_x x + m\phi - \omega t)} \tag{2.11}$$

where ϕ is the azimuthal angle, m is the azimuthal periodicity of the pressure perturbation, k_x is the axial wavenumber and ω is the radian frequency. Application of Eq. (2.11) to Eq. (2.9) determines an expression for the radial pressure dependence as

$$\frac{R_m''}{R_m} + \frac{1}{r}\frac{R_m'}{R_m} - \left(\frac{m}{r}\right)^2 = \left[2Mk_x\left(\frac{\omega}{a}\right) - \left(\frac{\omega}{a}\right)^2 - \left(M^2-1\right)k_x^2\right] \tag{2.12}$$

where $M = U/a$ is the flow Mach number. Defining the acoustic wavenumber as $k_a = \omega/a$ the radial dependence becomes

$$\frac{R_m''}{R_m} + \frac{1}{r}\frac{R_m'}{R_m} - \left(\frac{m}{r}\right)^2 = \left[2Mk_xk_a - k_a^2 - \left(M^2-1\right)k_x^2\right] = -k_r^2 \tag{2.13}$$

where k_r is the radial wavenumber. Since the right and left hand sides depend on variables independent of each other the radial wavenumber k_r must be a fixed constant. The radial dependence in Eq. (2.12) can then be written as

$$R_m'' + \frac{1}{r}R_m' + \left[k_r^2 - \frac{m^2}{r^2}\right]R_m = 0 \tag{2.14}$$

Eq. (2.14) takes the form of the Bessel equation with the known solution

$$R_m(r) = A_m J_m(k_r r) + B_m Y_m(k_r r) \tag{2.15}$$

where J and Y are the Bessel functions of the first and second kind. Application of the bound-

ary condition at the inner and outer duct radii constrains the available radial wavenumbers $k_{r,mn}$ by the relation

$$J'_m(k_{r,mn}R_i)Y'_m(k_{r,mn}R_o) - J'_m(k_{r,mn}R_o)Y'_m(k_{r,mn}R_i) = 0 \tag{2.16}$$

where J'_m and Y'_m are the derivatives of the Bessel functions of the first and second kind, respectively, and are of order m. Superimposing the solutions for all the azimuthal and radial modes of the eigenfunctions gives the complete tonal pressure field as

$$p(z, r, \phi, t) = e^{-i\omega t} \sum_{m=-\infty}^{\infty} \sum_{n=0}^{\infty} [A_{mn}J_m(k_{r,mn}r) + B_{mn}Y_m(k_{r,mn}r)]e^{i(k_{x,mn}x+m\phi)} \tag{2.17}$$

where B_{mn} is related to A_{mn} through application of the boundary condition at the duct walls.

For an azimuthal mode $m = 0$ there is no angular variation in the sound pressure but, for a fixed axial wavenumber, the term $e^{i(m\phi-\omega t)}$ describes wavefronts that form a helical pattern propagating downstream.

2.3 Tyler-Sofrin Modes

A key artifact of Eq. (2.17) is that the internal acoustic field of a rotating fan is given by a sum of modes, each defined by the product of separable radial, axial and azimuthal eigenfunctions. An important question therefore becomes: under a specified operation condition, what modes will persist within the duct and what modes will decay?

Observing the axial pressure dependence, it becomes evident that if the axial wavenumber is real, the resulting sound field will be given by oscillatory waves that propagate unattenuated with a phase speed of $c_x = \omega/k_x$. For these specific axial wavenumbers the tonal components

are called *cut-on* modes. Conversely, if k_x is imaginary, the waves will decay exponentially and are called *cut-off* or *evanescent* modes.

Observing the right-hand side of Eq. (2.12) one obtains a constraint for the axial wavenumber as

$$k_{x,mn} = \frac{k_a}{1-M^2}\left[-M \pm \sqrt{1-(1-M^2)\left(\frac{k_{r,mn}}{k_a}\right)^2}\right] \tag{2.18}$$

Eq. (2.18) is a dispersion relation between the axial and radial wavenumbers. For a given frequency (acoustic wavenumber k_a), the cut-on status of a mode depends on the radial wavenumber and the flow Mach number. A complete list of the available radial wavenumbers is set through Eq. (2.16). However, to utilize this condition, one must first have some a priori knowledge regarding the azimuthal mode number.

Following the analysis of Sofrin and Tyler [10], the azimuthal mode number within the duct can be obtained from the geometry of the fan components. A brief summary of their analysis is provided. The disturbance the rotating blades impose on the flow results in a periodic pattern aft of the rotor with a radian frequency given by Eq. (2.8). The azimuthal periodicity of this pattern is given by $2\pi/(n_{BPF}B)$ meaning that the azimuthal pattern (mode number) created by the rotor is

$$m_{rotor} = n_{BPF}B \quad , \; n_{BPF} = 1, 2, ... \tag{2.19}$$

Most ducted fan designs include stators near the duct exit which will further disturb the azimuthal periodicity of the flow. For a stator containing V stator vanes, the pressure perturbations generated from the flow hitting the stator vane will result in an azimuthal pattern with a mode number of

$$m_{stator} = cV \quad , \; c = ..., -2, -1, 0, 1, 2, ... \tag{2.20}$$

The inclusion of both negative and positive values of c indicates that the pattern can rotate clockwise or counterclockwise. The total azimuthal periodicity of the exiting acoustic field is the sum of the rotor and stator modes and is given by

$$m = n_{BPF}B + cV \tag{2.21}$$

with $n_{BPF} = 1, 2, ...$ and $c = ..., -2, -1, 0, 1, 2, ...$ The combination of equations (2.16), (2.18) and (2.21) result in a criterion for the cut-on status in terms of the duct Mach number M and radial wavenumber $k_{r,mn}$ for a mode defined by azimuthal order m and radial order n. The cut-on criterion is summarized as

$$k_{r,mn}\sqrt{1-M^2} \begin{cases} < k_a, & \text{mode is CUT-ON} \\ \geq k_a, & \text{mode is CUT-OFF} \end{cases} \tag{2.22}$$

2.4 Tonal Aft Emission Model

The complete acoustic field can be divided into two distinct regions. The first region contains all acoustic sources and within this zone, the field becomes extremely complex. However, outside of this region, linear propagation in a quiescent medium with a constant speed of sound is governed simply by the wave equation. Leveraging this spatial decomposition, one can attempt modeling the complete acoustic field by prescribing a pressure surface between the source region and the quiescent medium. The prescribed surface can then be used in conjunction to already developed solvers for acoustic propagation, such as boundary element method (BEM) [29], to solve for the acoustic field. The shape of the prescribed pressure surface, also called the radiating surface, is arbitrary and can take on any convenient shape for modelling the source. The benefit of the surface based model originates from its computation efficiency, which is orders of magnitude lower than standard high fidelity simulations.

Inspired by previous efforts undertaken by Papamoschou in jet noise modeling [25, 26], both Papamoschou and Truong proposed a promising surface-based modelling approach for the prediction of aft-emitted tonal fan noise [1, 23]; the distinction here being that unlike jet noise, tonal fan noise is deterministic. The resulting surface model prescribes a collection of waveforms on a cylindrical near-field surface taken at a radius equal to the exit-radius of the fan duct as shown in figure 2.2. The axial coordinate x is taken as zero at the fan exit plane and the radial coordinate, r, is defined from the fan centerline.

The waveforms prescribed on the source surface are informed by the internal duct acoustics discussed in Sections 2.2 and 2.3. Each waveform corresponds to the predicted cut-on Tyler-Sofrin modes and is assumed to maintain the same azimuthal order m as the cut-on mode. Computational results for aft fan noise by Huang *et al.* [18] show an emission pattern similar to Mach wave emission in jets that motivates maintaining the initial convective Mach number close to the value obtained through internal duct acoustics. The convective Mach number is associated with the wavenumber through

$$M_{c,mn}(0) = \frac{k_a}{k_{x,mn}(0)} \tag{2.23}$$

and can be connected to the polar emission via

$$\theta_{mn} = \arccos\left(\frac{1}{M_{c,mn}}\right) \tag{2.24}$$

The convective Mach number is assumed to decay by

$$M_c(x) = 1 + (M_c(0) - 1)\mathcal{D}(x) \tag{2.25}$$

where $\mathcal{D}(x)$ is a decay function. Note that this enforces that the convective Mach number decays to the speed of sound at some distance from the nozzle as one would expect. The

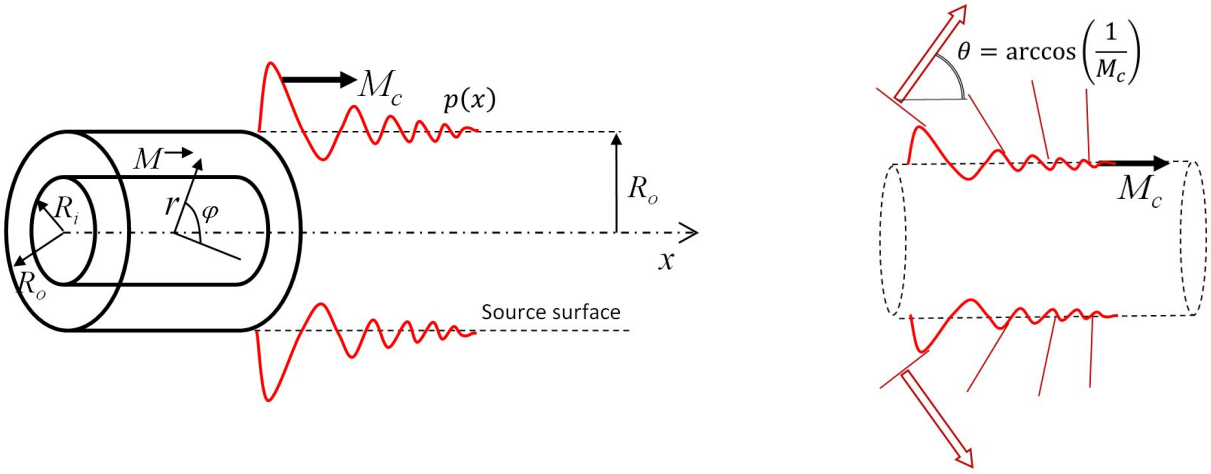

Figure 2.2: Source surface setup for modeling of aft-tonal noise emissions from Ref. [1].

axial wavenumber is then determined by

$$k_x(x) = \frac{k_a}{M_c(x)} \tag{2.26}$$

The decay function is chosen as

$$\mathcal{D}(x) = \exp\left[-g\left(\frac{x}{R_o}\right)^h\right] \tag{2.27}$$

where g and h are free parameters. Assuming that the waveform decays similar to the convective Mach number the waveform shape can be expressed as

$$p_{mn}(x,\phi) = A_{mn}\mathcal{D}_{mn}(x)e^{ik_{x,mn}(x)x+im\phi} \tag{2.28}$$

To determine the axial evolution of a given waveform one therefore only needs to define the parameter vector

$$\mathbf{z}_{mn} = [A_{mn}, M_{c,mn}(0), g_{mn}, h_{mn}] \tag{2.29}$$

The amplitude A is complex and the total parameter vector therefore contains five elements

for each mode. The complete surface-based source is therefore given by the coherent summation of all the waveforms:

$$p_{source}(\mathbf{Z}; x, \phi) = \sum_{(m,n)} p_{mn}(\mathbf{z}_{mn}; x, \phi) \tag{2.30}$$

where (m, n) indicates the summation over the cut-on modes and

$$\mathbf{Z} = [\mathbf{z}_{mn}] \tag{2.31}$$

is the overall parameter vector.

Outside the source surface, each waveform p_{mn} can be propagated to any desired field point (x, r, ϕ). For the chosen cylindrical source surface, the solution to the wave equation gives the emitted pressure field

$$P_{mn}(\mathbf{z}_{mn}; x, r, \phi) = \frac{e^{im\phi}}{2\pi} \int_{-\infty}^{\infty} \hat{p}_{mn}(\mathbf{z}_{mn}, \kappa_x, \phi) \frac{H_m^{(1)}(\kappa_r r)}{H_m^{(1)}(\kappa_r R_o)} e^{i\kappa_x x} d\kappa_x \tag{2.32}$$

κ_x and κ_r are the axial and radial wavenumbers associated with outward propagation in a quiescent medium and are related to the acoustic wavenumber by $k_a^2 = \kappa_x^2 + \kappa_r^2$; $\hat{p}_{mn}$ is the axial Fourier transform of p_{mn} and $H_m^{(1)}$ is the Hankel function of the first kind of order m. One can obtain the complete pressure field from the superposition

$$p(\mathbf{Z}; x, r, \phi) = \sum_{(m,n)} P_{mn}(\mathbf{z}_{mn}; x, r, \phi) \tag{2.33}$$

The cut-on modes for the 2^{nd} and 3^{rd} harmonic of the ducted fan rig described in chapter 4 were determined from the Tyler-Sofrin analysis in section 2.3 and are listed in Tables 2.1 and 2.2 respectively.

The parameter vector $\mathbf{Z}$ was determined by minimizing the difference between the modeled

Table 1. Cut-on modes for $n_{BPF} = 2$

(m, n)	(4,1)	(4,2)
$k_x(0)$ (m^{-1})	309	179
$M_c(0)$	1.53	2.64
θ (deg)	49.2	67.8

Table 2.1: Parameter specifications for the cut-on modes of the 2^{nd} harmonic.

Table 2. Cut-on modes for $n_{BPF} = 3$

(m, n)	(-6,1)	(-6,2)	(18,1)
$k_x(0)$ (m^{-1})	462.0	380	246
$M_c(0)$	1.53	1.86	2.87
θ (deg)	49.2	57.4	69.5

Table 2.2: Parameter specifications for the cut-on modes of the 3^{rd} harmonic.

and experimental cross-spectral densities in the far-field. Figures 2.3 and 2.4 show the results for the parameterization for $n_{BPF} = 2$ and $n_{BPF} = 3$ respectively. For $n_{BPF} = 2$ the dominant waveform, denoted by the black line in the top of Fig. 2.3 corresponds to mode (4,1) and has a peak radiation at a polar angle $\theta = 47°$. For $n_{BPF} = 3$ the dominant waveform denoted by the black line in the top of Fig. 2.4 corresponds to mode (18,1) and has a peak radiation at $\theta = 68°$. For both harmonics the remaining cut-on modes are much weaker than the dominant mode. A central question of this work is whether this source formulation based on far-field data can give accurate results in the near field.

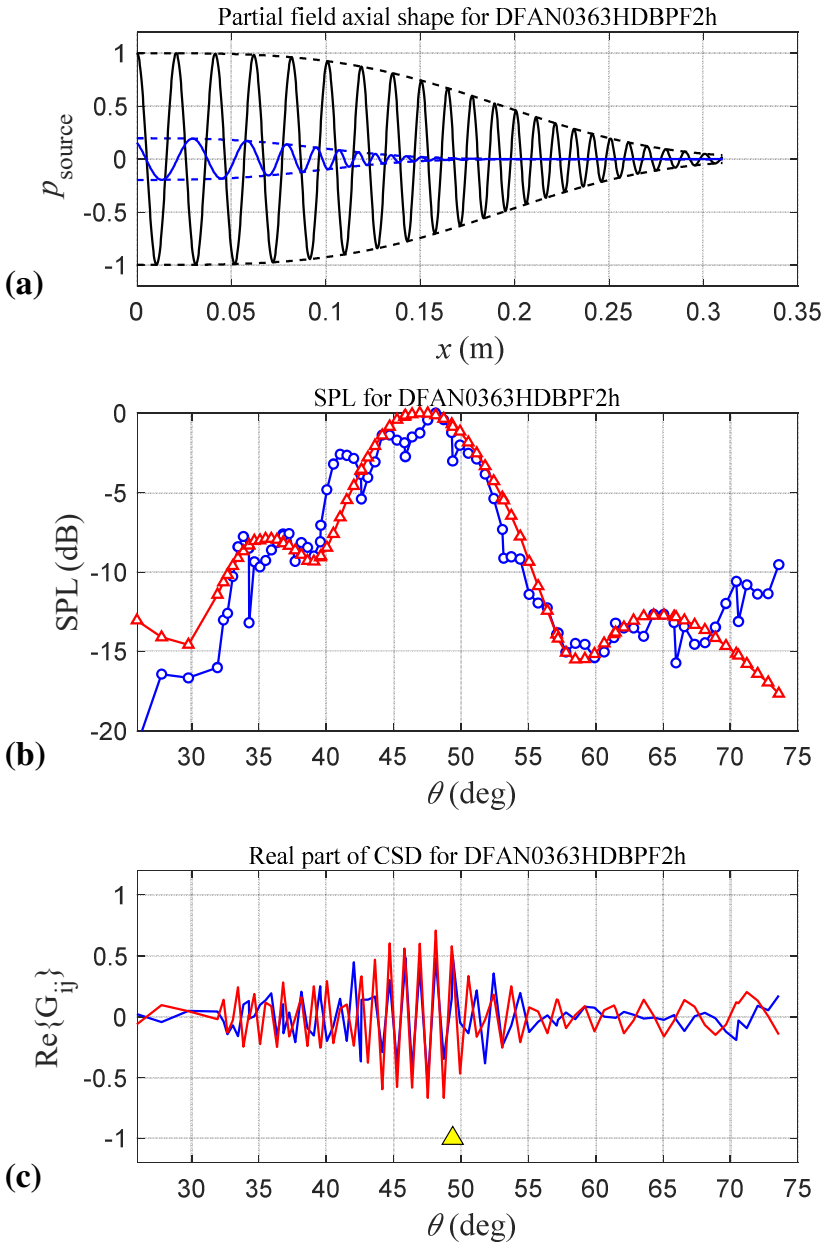

Figure 2.3: Source parameterization for $n_{BPF} = 2$ based on far-field phased array measurements. Top row: source waveforms; middle row: directivity of SPL for experiment (blue) and model (red); bottom row: directivity of real part of cross-spectral matrix for experiment (blue) and model (red), with reference sensor at $\theta = 48°$. From Ref. [1].

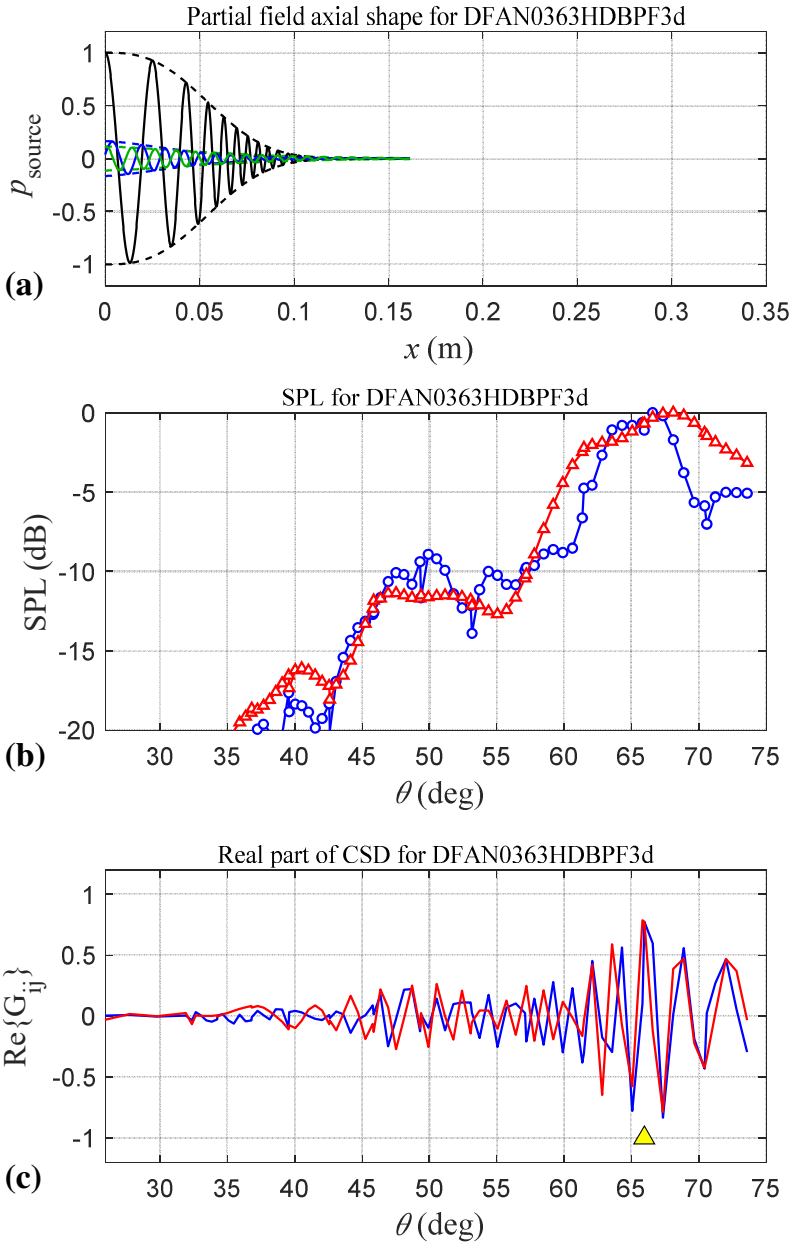

Figure 2.4: Source parameterization for $n_{BPF} = 3$ based on far-field phased array measurements. Top row: source waveforms; middle row: directivity of SPL for experiment (blue) and model (red); bottom row: directivity of real part of cross-spectral matrix for experiment (blue) and model (red), with reference sensor at $\theta = 66°$. From Ref. [1].

Chapter 3

Signal Processing

Phased microphone arrays have become the standard method for obtaining acoustic measurements and are comprised of a system of spatially-distributed sensors that take simultaneous measurements of sound pressure. The relative amplitudes and phase differences between sensor measurements are utilized to determine the location of noise sources within a field and can be used to deduce the leading mechanisms of sound generation within the flow. The procedure of properly adjusting these recorded signals is known as beamforming. This chapter outlines the foundational methods developed for the beamforming of deterministic signals using a traditional fixed microphone array. The analysis will cover both a frequency and a time domain approach to beamforming. The methods will then be extended to microphone arrays combining both fixed and continuously-scanning sensors.

3.1 Time Domain Analysis

Consider a series of sensors placed at a spatial coordinate $\mathbf{x} = (x, r, \phi)$. The resulting signal $p(\mathbf{x}, t)$ is a time-series measurement of the pressure fluctuation. Noise localization techniques

involve adjusting each individual microphone's signal using time delays that are dependent on the relative position between the source and the microphone. In this manner, information about the source can be obtained; however, as discussed in section 2.1, the measured pressure field contains contributions not only from the tonal content but from the broadband spectrum as well. Therefore, to properly assess the contribution of an individual harmonic to the pressure field, one must first extract the tonal contributions from the complete signal. Once the harmonic contributions have been isolated, standard beamforming techniques can then be utilized to characterize the noise source.

3.1.1 Vold-Kalman Filter

Methods of extracting a tonal component's time series from a sensor's raw measurements has been heavily researched and previous work performed at the UCI anechoic facility has focused particularly on the use of the Vold-Kalman (VK) filter [30–32].

The VK filter was introduced by Vold and Leuridan [30] and extracts the non-stationary tonal components of a deterministic signal by tracking a known frequency vector throughout the complete experiment duration. Tonal fan noise is deterministic and when operating with a constant blade number, the tone frequency becomes dependent solely upon fan RPM. Therefore, with the use of a tachometer, a reference frequency vector can be recorded to track the fundamental blade passing frequency and separate each harmonic from the complete acoustic spectrum.

The output of the VK filter is a time-domain signal containing the same number of samples as the raw trace; however, the filtered data now contain the sole contribution of each harmonic to the complete acoustic field. After separating each tone's contributions, other signal processing methods can then be leveraged to gain insight on the sound generation mechanisms surrounding a given tone.

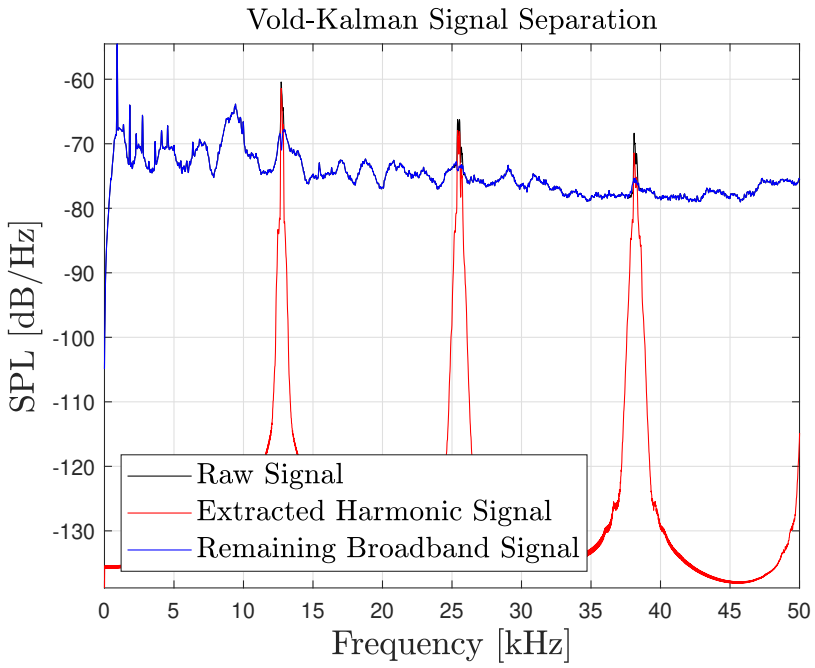

Figure 3.1: Sample of the spectral densities of the original signal and its harmonic and broadband components separated by the Vold-Kalman filter.

An example of the separation of the tonal acoustic field from the broadband spectrum is provided in Fig. 3.1 for the axial scanning experiments outlined in section 4.3. An extensive review of the VK filter is found in Ref. [23].

3.1.2 Space-Time Correlations

Noise-source localization is based on knowing the relationship between simultaneously measured pressures at spatially-phased locations. For an acoustic wave, this relationship can be described in terms of the relative amplitude and phase differences between measurements. Provided these relationships are known with a sufficient resolution one can then use these relationships to trace the acoustic waves throughout the field and obtain key details about how the observed noise emissions are generated.

These relationships are computed quantitatively through the cross-correlation coefficient, R.

The cross-correlation is in general, complex valued and for a time-series measurement the normalized cross-correlation is expressed as

$$R(\mathbf{x}, t; \mathbf{x} + \boldsymbol{\xi}, t + \tau) = \frac{< p(\mathbf{x}, t) p^*(\mathbf{x} + \boldsymbol{\xi}, t + \tau) >}{|p(\mathbf{x}, t)||p(\mathbf{x} + \boldsymbol{\xi}, t + \tau)|} \tag{3.1}$$

where $\mathbf{x} = (x, r, \phi)$ is a reference spatial location, $\boldsymbol{\xi} = (\xi, \rho, \Delta\Phi)$ is the spatial distance from the reference location, t is the reference measurement time, τ is the time lag from the reference time, $*$ denotes the complex conjugate and $< . >$ denotes the time average. For a harmonic signal, the sound pressure can be expressed as

$$p(\mathbf{x}, t) = P(\mathbf{x}) e^{-i\omega t} \tag{3.2}$$

where P is the complex amplitude (phasor) of the sound pressure. The normalized cross-correlation can therefore be expressed as

$$R(\mathbf{x}; \boldsymbol{\xi}, \tau) = \frac{P(\mathbf{x}) P^*(\boldsymbol{x} + \boldsymbol{\xi})}{|P(\mathbf{x})||P(\mathbf{x} + \boldsymbol{\xi})|} e^{i\omega\tau} \tag{3.3}$$

The relative amplitude between signals is given by the real component of the cross-correlation and the phase difference $\Delta\psi$ between signals is given by the angle between the imaginary and real components of the cross-correlation.

$$\Delta\psi = \arctan\left(\frac{Im[R]}{Re[R]}\right) \tag{3.4}$$

The analytical solution to the internal pressure field of a fan placed in an annular duct is given by Eq. (2.17), which showed that the sound pressure could be decomposed into separable azimuthal, radial and axial components. From the definition of the cross-correlation, one can therefore realize that for sensors placed at a constant radius and axial position, the azimuthal periodicity, m, of the acoustic field can be determined from the azimuthal spacing

between peak correlation values $\Delta\phi_{peak}$ by $m = 2\pi/\Delta\phi_{peak}$. Here the normalized azimuthal correlations are given by

$$R(\phi; \Delta\phi, \tau) = \frac{P(\phi)P^*(\phi + \Delta\phi)}{|P(\phi)||P(\phi + \Delta\phi)|} e^{i\omega\tau} \tag{3.5}$$

Similarly, for sensors located at a constant radius and azimuthal angle, the axial wavenumber and therefore convective Mach number, can be determined from the axial correlation values. Here the normalized axial correlation is given by

$$R(x; \xi, \tau) = \frac{P(x)P^*(x + \xi)}{|P(x)||P(x + \xi)|} e^{i\omega\tau} \tag{3.6}$$

3.2 Frequency Domain Analysis

Similarly to the definition of the power spectral density in Eq. 2.5, the cross-spectral density (CSD) between sensors i and j is

$$S_{ij}(\omega) \;=\; \overline{\widehat{p}_i(\omega)\widehat{p}_j^*(\omega)} \tag{3.7}$$

It represents, approximately, the Fourier transform of the unnormalized cross-correlation of Eq. (3.1), with sensor i at $\mathbf{x}$ and sensor j at $\mathbf{x} + \xi$. The CSD can be based on the full signal or a harmonic of the signal extracted using the VK filter. The CSD is generally complex-valued with the real component representing the similarity of the in-phase signals and the imaginary component representing the similarity of the out-of phase signals. The phase difference between two sensor measurements can be obtained from the CSD as

$$\Delta\psi(\omega) = \arctan\left(\frac{Im[S_{ij}(\omega)]}{Re[S_{ij}(\omega)]}\right) \tag{3.8}$$

Obtaining a detailed depiction of the acoustic field requires a spatially dense array of measurements and therefore numerous cross power spectral densities. It becomes useful to organize this information in matrix form. The resulting matrix is called the cross-spectral matrix (CSM) and contains the cross-spectral densities between all sensor pairs. The CSM is one of the most powerful tools used in acoustic analysis. The CSM stores each CSD in the matrix bin corresponding to the sensor deployments (e.g. the CSD between sensors 1 and 2 is stored in the matrix bin (1,2)) with the auto-spectral densities along the matrix diagonal. The CSM is a Hermitian matrix.

3.3 Continuous-Scan Beamforming

Accurate imaging of aeroacoustic sources generally requires a spatial resolution that can only be obtained through advanced setups, such as the use of continuously scanning sensors. While the resolution obtained utilizing the continuous scan method is significantly greater than traditional setups, the induced motion of the sensor through a non-stationary field introduces new challenges that must be accounted for when processing the sensor's raw signal. Previous efforts by Papamoschou and Morata [27] have proposed general methods to account for these challenges. A brief summary of these methods is provided below.

In general, the acoustic field is spatially non-stationary and for a traversing sensor, this means that the acoustic features captured by the sensor at the beginning of the experiment will be different from those captured at the end. The significance of this deviation can be expressed in terms of the non-dimensional parameter $V_m T/X$, where V_m is the sensor speed, T is the duration of the sensor movement and X is the length scale of the spatial variation in the acoustic field. In addition to the spatial variance, the sensor velocity relative to the acoustic source will cause the measured signal to experience a Doppler-shifted frequency that is dependent upon the sensor's Mach number V_m/a.

The third challenge faced when processing the data from a scanning sensors results from the decrease in acoustic wavelength with an increase in acoustic frequency. As demonstrated in section 3.1.2, the length scale of the correlation field for a harmonic signal will vary proportionally to the measured frequency and for a given scan speed, this means the sensor's displacement with respect to the correlation field will depend on the resolved frequency. The significance of this displacement can be approximated by $V_m T/\lambda$, where λ is the acoustic wavelength.

The three dimensionless groups: $V_m T/X$, V_m/a and $V_m T/\lambda$ serve as broad measures of non-stationarity in the field and if all quantities remain small, then the signal processing techniques provided in sections 3.1.2 and 3.2 will provide accurate measurements of the acoustic field. To reduce the effect of the spatial non-stationarity, the complete signals of the scanning sensors are divided into smaller blocks, over which the signals and their correlations can be considered quasi-stationary. For each block, the sensor location is taken as the geometric mean of the block location. After the block division, the Doppler-shifted frequency can be corrected for by tracking the sensor velocity throughout the duration of the experiment. Lastly, the frequency dependent correlation field is accounted for by dynamically adjusting the number of samples used in spectral estimation based on the resolved frequency. The frequency window used within this work follows a Gaussian distribution and utilizes the parameter selection suggested by Papamoschou and Morata [27].

3.4 Partial Fields Decomposition

Section 3.3 outlined techniques for suppressing spatial non-stationarity within continuous-scan measurements such that the cross-spectral densities between sensors of the same block could be computed. The result is a series of cross-spectral sub-matrices each corresponding to an individual block. However, due to the sparse location of the scanning sensors, the

constructed sub-matrices are by themselves, not inherently useful. Instead, one seeks to obtain a singular densely-populated global CSM by patching together the contributions of each individual sub-matrix. Accurate construction of a global CSM for continuous scan arrays has been extensively researched [5] and previous work on source localization of tonal jet and fan noise has motivated the current investigation to construct a global CSM using Partial Fields Decomposition (PFD) [21, 33, 34].

The premise of the PFD technique is to decompose the acoustic field into a set of coherent and mutually orthogonal partial fields. Each partial field corresponds to the pressure contribution of an independent source to the complete measured pressure field. The independent sources are obtained through the singular value decomposition (SVD) of a reference CSM. Considering a set of fixed sensors F and a set of continuously scanning sensors S, the reference CSM $\mathbf{G}_{FF}$ is constructed from the full time trace of the fixed sensors only:

$$\mathbf{G}_{FF}(\omega) = \overline{\hat{p}_i(\omega)\hat{p}_j^*(\omega)}, \quad (i,j) \in F \tag{3.9}$$

where $\overline{(\cdot)}$ indicates the operation used for spectral averaging and $*$ denotes the complex conjugate. The reference matrix has the SVD

$$\mathbf{G}_{FF}(\omega) = \mathbf{U}_{FF}\mathbf{\Sigma}_{FF}\mathbf{V}_{FF}^H \tag{3.10}$$

where the matrix $\mathbf{\Sigma}_{FF}$ contains the singular values of the reference matrix $\mathbf{G}_{FF}$. The singular values are a measure of each source's contribution to the complete pressure field. Once the acoustic field has been decomposed, then the stationary sensors can be used as phase references for each of the decomposed sources. Computation of the correlations between the scanning sensors requires that the signal is divided into K blocks with the position of the scanning sensors computed at the center of each block. For each block two cross-spectral

matrices are constructed: a CSM between the fixed sensors $\mathbf{G}_{FF,k}$

$$\mathbf{G}_{FF,k} = \overline{\hat{p}_{i,k}(\omega)\hat{p}^*_{j,k}(\omega)}, \quad (i,j) \in F \tag{3.11}$$

and a CSM between fixed and scanning sensors

$$\mathbf{G}_{FS,k} = \overline{\hat{p}_{i,k}(\omega)\hat{p}^*_{j,k}(\omega)}, \quad i \in F, \quad j \in S \tag{3.12}$$

To reduce the effects of non-stationarity, a frequency dependent filter is applied in the estimation of the cross-spectral densities. A transfer matrix between the fixed and scanning sensors is then constructed for each block as

$$\mathbf{H}_{FS,k} = \left(\mathbf{G}_{FF,k}\right)^{-1} \mathbf{G}_{FS,k} \tag{3.13}$$

Fig. 3.2 demonstrates the generation of the transfer matrix. A potential difficulty is that $\mathbf{G}_{FF,k}$ may not have an inverse in which case the Moore-Penrose generalized inverse is used:

$$\left(\mathbf{G}_{FF,k}\right)^{-1} = \left(\mathbf{G}_{FF,k}\right)^{\dagger} = \mathbf{V}_{FF,k}\mathbf{\Sigma}^{-1}_{FF,k}\mathbf{U}^{H}_{FF,k} \tag{3.14}$$

The partial fields for block k are then computed as

$$\mathbf{\Pi}_k = \mathbf{H}^{T}_{FS,k}\mathbf{U}_{FF}\mathbf{\Sigma}^{1/2}_{FF} \tag{3.15}$$

where superscript T indicates the transpose. Noting that each block k represents a distinct axial location x_k, for a dense block distribution the partial fields can be approximated as

$$\Pi_k \approx \Pi(x) \tag{3.16}$$

A global CSM with size $K\mathcal{M}_S$x$K\mathcal{M}_S$, where $\mathcal{M}_S$ is the number of scanning sensors, is obtained from

$$\mathbf{G}_{PFD} = \mathbf{\Pi}_{\alpha}^{H}\mathbf{\Pi}_{\beta}, \quad \alpha, \beta = 1, ..., K \tag{3.17}$$

In addition to generating a global CSM, a singular partial field $\Pi(x)$ along the scan line can be used to construct a cylindrical surface of radius r where the pressure field has the form

$$p(x, r, \phi, t) = \Pi(x)e^{-i\omega t}e^{im\phi} \tag{3.18}$$

This pressure can be used as a boundary condition in the boundary element method to propagate sound and predict far-field emissions [29].

Note that when decomposing the the acoustic field into individual coherent sources, the SVD of the reference CSM $\mathbf{G}_{FF}$ was used. This means that the number of decomposed individual sources is equivalent to the number of reference sensors used during the experiment. To adequately describe the acoustic field, it is therefore important that more reference sensors are used than number of sources present in the flow. Additionally, one should be careful to make sure that the number of partial fields (each corresponding to a reference sensor) used in constructing the global CSM captures the majority of the energy at the frequency of interest in the flow.

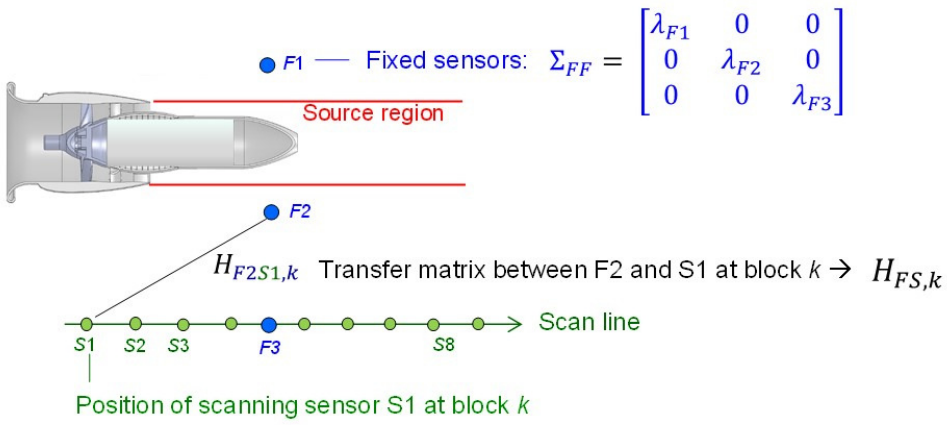

Figure 3.2: Generation of acoustic transfer matrix for phase reference utilized in partial field decomposition.

Chapter 4

Experimental Setup

This chapter outlines the experimental program used when conducting the acoustic measurements presented in this work. A description of the anechoic chamber, near-field microphone array, sensor tracking system and small-scale ducted fan are provided along with the specific conditions for all conducted experiments.

4.1 Anechoic Chamber and Microphone Array

All experiments were conducted inside the UCI anechoic chamber, depicted in Fig. 4.1. The facility has an internal volume of approximately 990 ft^3 with the complete inner surface covered in acoustic foam wedges. The wedges have been arranged to mitigate wave reflections. The sensor deployment utilizes Bruel and Kjaer Model 4138 1/8-inch condenser microphones with a frequency resolution of 120kHz. The microphones are connected to six conditioning amplifiers sampled simultaneously at 250kHz by three NI PCI-6143 data acquisition boards. The acquisition boards are installed in a PC with an Intel i7-7700K quad-core processor. Data collection is controlled through Labview.

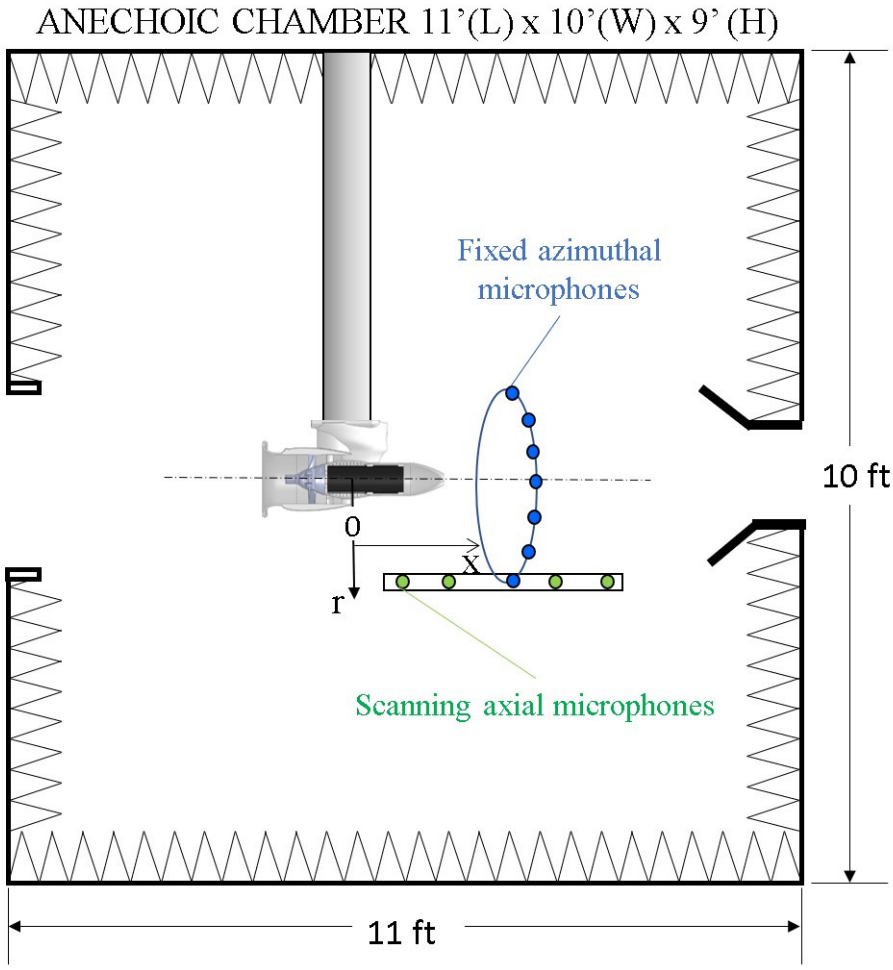

Figure 4.1: Schematic of the UCI anechoic facility integrated with a small-scale ducted fan and near-field microphone array.

Temperature and relative humidity are recorded throughout the duration of the experiment to allow for the computation of the exact speed of sound. The microphone signals are filtered with a high-pass filter set at 350Hz to mitigate possible DC noise signals.

The near-field microphone array combines a scanning axially-phased array with a stationary azimuthally-phased array and is depicted in Fig. 4.2. The microphone arrays are constructed from polylactic acid (PLA) using fused deposition modeling on an Ender 3-pro 3D printer with a resolution of $\pm 0.1mm$. The azimuthal ring is placed parallel to the fan exit plane and can be adjusted to various desired axial locations. The maximum azimuthal resolution is

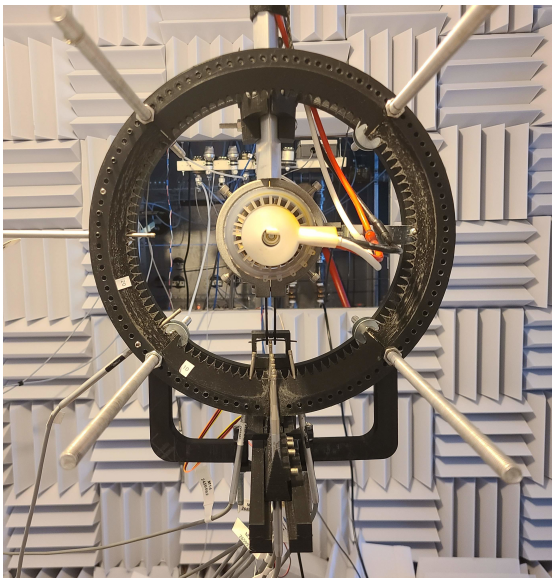

(a) Front-view

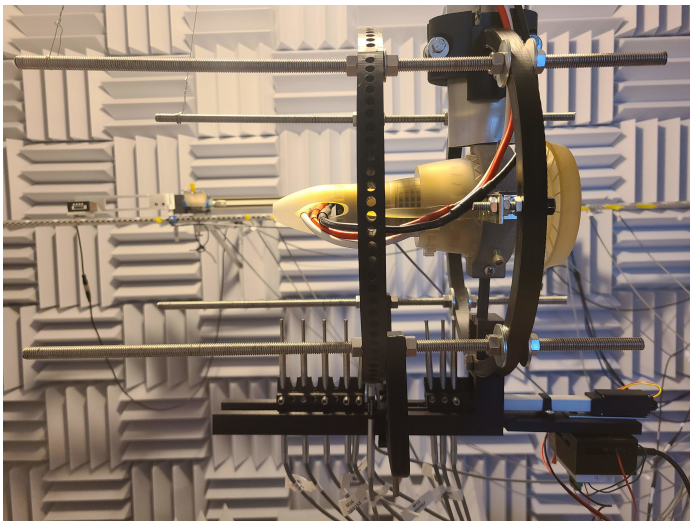

(b) Side-view

Figure 4.2: Integration of small-scale ducted fan rig with the near-field array in the UCI anechoic chamber.

$\Delta\phi = 3.6°$. The scanning array traverses the axial coordinate and is powered by an Actuonix L-16P linear actuator. The entire array configuration was mounted to the swing arm of the fan to maintain proper orientation with respect to the fan throughout the duration of the experiment.

The position of the scanning sensors must be monitored to ensure that the microphone trajectories are properly synced with the pressure signals. Sensor synchronization and position signals are recorded simultaneously with the pressure time traces throughout the duration of the experiment and are constructed from splitting the voltage input of the scanning sensor motor (L-16P mini linear actuator) and directing it towards a channel on the data acquisition board (DAQ). A high-pass 350 Hz filter is also applied to the signal to remove potential DC signal noise. The activation and termination of the scanning sensor is determined by detecting the instant where a peak voltage value for the synchronization signal is found. The data acquired outside of the activation and termination window is disregarded. Figure 4.3 shows an example of a pressure and synchronization signal for the axially scanning experi-

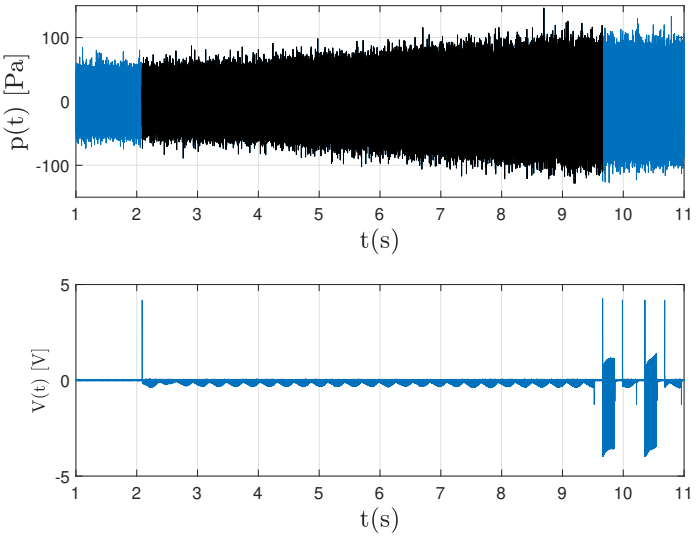

Figure 4.3: Example of microphone trace synchronization with the position. Pressure signal (top); Synchronization signal (bottom).

ment described in section 4.3. The stop and start points are clearly seen. Additional voltage spikes are also observed after the initial stop of the actuator. These spikes are a result of some oscillatory motion by the actuator at the end of the scan region; however, the data within this region is disregarded such that it does not adversely effect the signal processing.

During the complete experiment run, all scanning sensors maintain a constant relative position to one another such that the position of each microphone can be determine through a recording of the actuator stroke length and a priori knowledge of the relative microphone spacing. The actuator stroke length is measured from a voltage reading ranging from 0 to 3.3V and is converted to distance based on its maximum stroke length of 100mm. An example tracking signal of the stroke length during an experiment run is shown in Fig. 4.4.

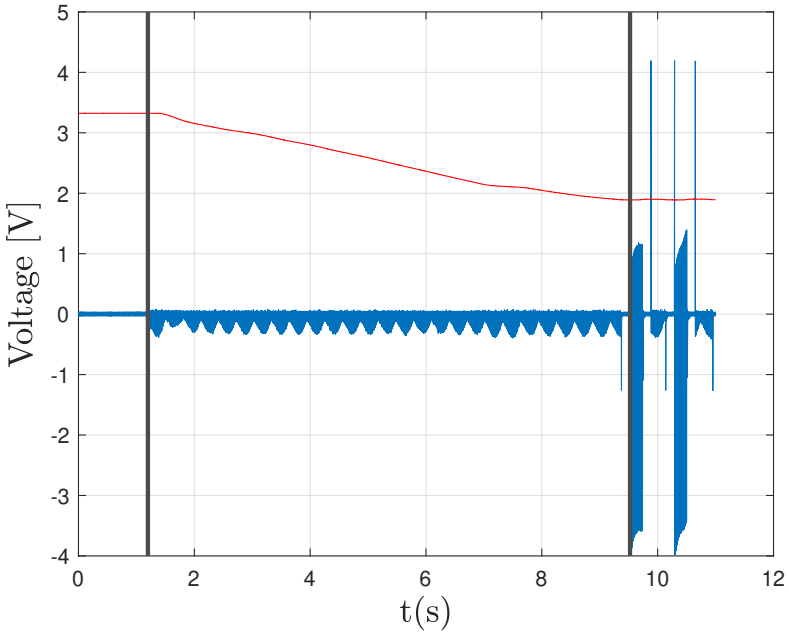

Figure 4.4: Stoke length of actuator (in Volts) relative to the synchronization signal

4.2 Ducted Fan

The conducted experiments utilized a small-scale ducted fan based on the GE R4 fan with a 14-bladed rotor and 24 stator vanes. The nacelle diameter at the rotor plane is 70 mm and the exit diameter of the fan duct is D_e =74 mm. The exit-to-inlet area ratio is 0.56. A schematic of the fan is provided in Fig. 4.5 and its detailed design is outlined in Ref. [23]. The fan is powered by a 6-hp DC brushless motor and yields a fan pressure ratio of 1.15. The tip Mach number reaches 0.59 when operated at 55000 RPM.

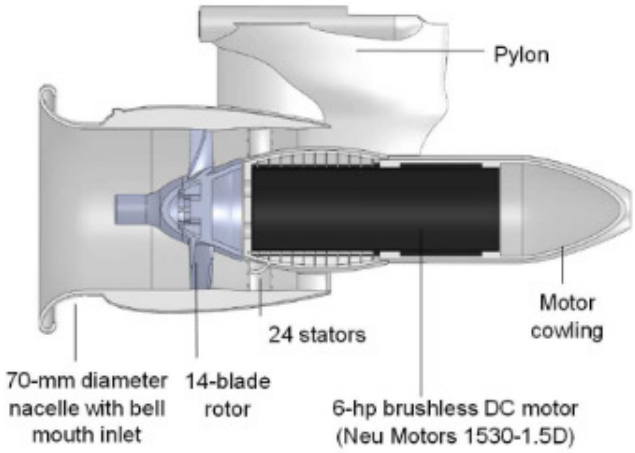

Figure 4.5: Schematic of small-scale GE R4 fan used for acoustic measurements in the UCI anechoic facility

4.3 Array Configurations

The near-field array depicted in Fig. 4.2 offers a vast range of possible sensor placements in both the axial and azimuthal deployments. For azimuthal measurements, it was sought to constraint this selection process by placing the ring of the azimuthal (fixed) sensors near the polar angle of peak emission for each respective harmonic. The peak emission is determined by the far-field SPL measurements, shown in Figs. 2.3 and 2.4. This corresponds to a polar angle of $\theta = 47°$ for measurements of $n_{BPF} = 2$ and $\theta = 68°$ for $n_{BPF} = 3$.

Azimuthal measurements were taken in isolation where the normalized coordinates $(x/D_e, r/D_e)$ for the sensor ring were (0.83, 0.88) and (0.56,1.53) for $n_{BPF} = 2$ and 3 respectively. For the investigation of $n_{BPF} = 2$, 12 sensors were used covering an azimuthal range of $-90° \leq \phi \leq 27°$. The predicted cut-on modes for $n_{BPF} = 3$ shown in table 2.2 have much finer features than for $n_{BPF} = 2$. The sensors were therefore placed over an azimuthal range of $-30.6° \leq \phi \leq 12.6°$ with a constant spacing of 3.6°. For both experimental runs, the run duration lasted 2s over which 500000 samples were acquired. The averaged RPM of the fan during operation was 52,900 and 53,300 for $n_{BPF} = 2$ and 3 respectively. Schematics of the

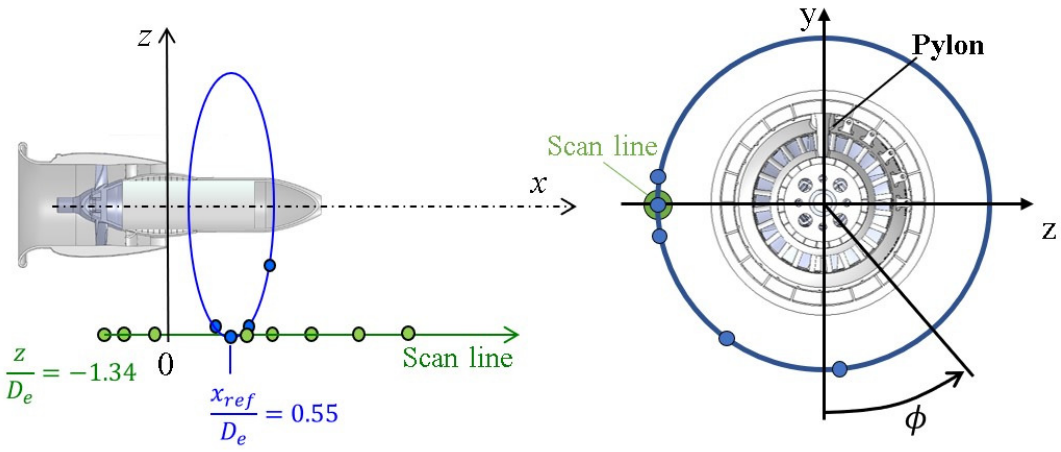

Figure 4.6: Schematic of microphone deployment used for axially scanning measurements

experimental setup are provided in Fig. 4.2.

For the axially scanning measurements, the fixed azimuthal ring was placed at a location that allowed for the greatest scan length while maintaining the fixed sensors near the peak emission regions. This corresponds to a sensor ring placement of $(x/D_e, r/D_e) = (0.55, 1.34)$. A total of five reference sensors were used for the scanning measurements. A single reference sensor was placed on the scan line ($\phi = -90°$) to serve as the reference sensor for axial correlations. Four additional sensors were mounted on the azimuthal holder to serve as a phase reference for PFD and were placed at $\phi = -182°, -142°, -99°$ and $-81°$. Eight scanning sensors were placed on the axially scanning traverse with three sensors fore and five aft of the fixed reference microphones. The axial spacing of the sensors ranged from 10 to 22mm. The experiment duration was 8 s over which 2000000 samples were acquired. The signal of each sensor was divided into $K = 40$ blocks with 15% overlap. Each block contained 60000 samples corresponding to a duration 0f 0.24s and a travel of 1.2mm. The averaged rotor RPM was 55,000. A schematic of the experimental setup is provided in Fig. 4.6

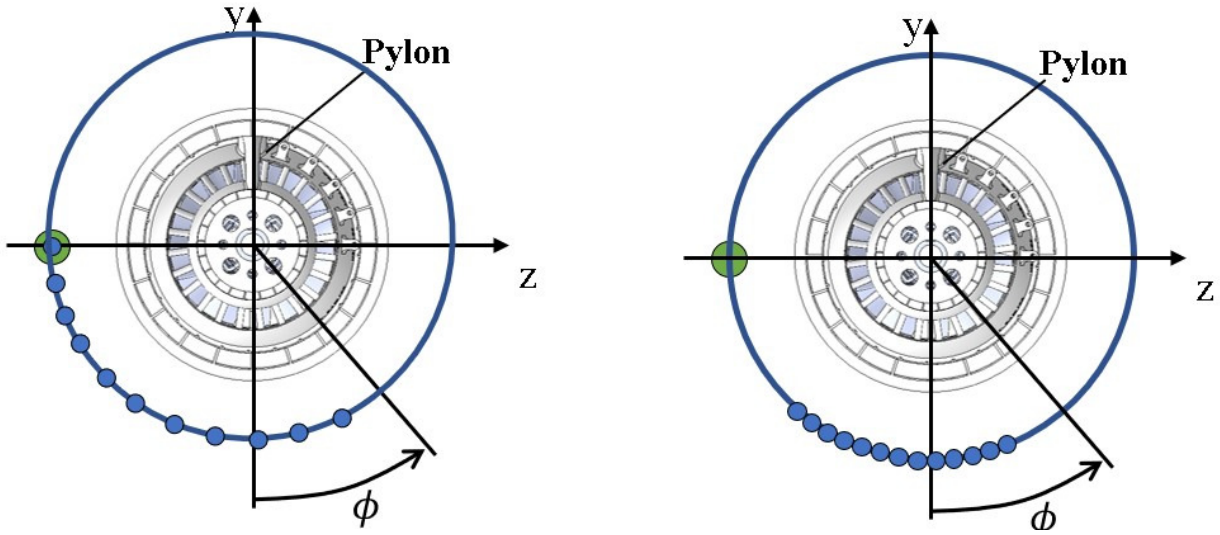

(a) (b)

Figure 4.7: Schematic of sensor deployments used for azimuthal measurements. Left: $n_{BPF} = 2$; Right $n_{BPF=3}$.

4.4 Processing of Harmonic Signals

Computation of the axial correlations and partial fields can result in a non-smooth distribution that complicates further processing e.g., the calculation of the convective Mach number. In addition the scanning setup discussed in section 4.3 has a spatial gap of about 5mm near the location of the azimuthal array. The array is placed in a sensitive area of the measurement and it is therefore necessary to smooth and interpolate the signals of interest. Considering a complex signal $p(x)$ that has a rapid oscillation, interpolation and smoothing of the real and imaginary parts yields highly unsatisfactory results. To overcome this challenge, the signal was expressed as

$$p(x) = |p(x)|e^{i\psi(x)} \tag{4.1}$$

where $\psi(x)$ is the unwrapped phase. Interpolation and smoothing of the amplitude $|p(x)|$ and unwrapped phase $\psi(x)$ were much more straight-forward and resulted in excellent reconstruction of the signal. The amplitude was reconstructed using a Fourier series and the

unwrapped phase was reconstructed using polynomial regression. This approach was applied to the partial field $\Pi(x)$ and to the axial correlation $Q(x, \xi)$ based on the VK-filtered signal.

Chapter 5

Near-Field Characterization of Tonal Fan Noise

The source model described in section 2.4 showed reasonable agreement to the far-field experimental measurements used for calibration however, as one moves closer to the source, additional mechanisms that were muted in the far-field become important. For the model to provide an accurate source prediction, it was of interest to ensure that the far-field parameterized model was capable of capturing the physics governing the acoustic near field. As discussed in section 2.4, several parameters defining the cut-on modes were assumed. The assumptions included the axial and azimuthal sound pressure distribution as well as each tone's convective Mach number distribution. To test the model's ability to accurately predict the near acoustic field, the following chapter will aim to compare these parameters to experimental measurements taken in the near field following the setup detailed in chapter 4. Since the model calibrations are currently provided for the $n_{BPF} = 2$ and 3, the validation will focus strictly on these two tones.

5.1 Azimuthal Mode Number

Each cut-on mode has a predicted internal azimuthal order according to the Tyler-Sofrin analysis described in section 2.3. In the model paramaterization, this theoretical mode number is assumed to be retained outside of the duct; however, it is important to verify whether this assumption is consistent with near-field pressure measurements.

The azimuthal order of the 2^{nd} harmonic will be investigated first. For the experiment conditions outlined in section 4.3, there are 2 predicted cut-on modes for $n_{BPF} = 2$, both containing an azimuthal order $m = 4$. Near-field measurements were obtained using the azimuthal sensor deployment for $n_{BPF} = 2$ and the harmonic content was extracted from the raw signals using the VK filter. The complete signal was divided into 100 segments each containing 5000 samples and the azimuthal correlations are computed from Eq. (3.5) then averaged over all segments. The resulting azimuthal correlations are plotted in Fig. 5.1 where the reference sensor has been chosen as the sensor located closest to the scan line. The near-field measurements have a peak correlation spacing of 95.4° which is consistent with an azimuthal order $m = 4$ (spacing of 90°) as predicted by duct acoustics. Though the predicted correlation spacing is consistent with the near-field measurements, there also appears to be a sporadic nature in the correlation field. This could possibly be a result of geometric disturbances such as the nacelle pylon or reflections induced by the experimental setup however, at this point a cause cannot be determined.

The azimuthal correlations are generated for the 3^{rd} harmonic using the azimuthal setup outlined for $n_{BPF} = 3$. The same procedure used for calculating the 2^{nd} harmonic is followed and the resulting correlations are provided in figure 5.1. For $n_{BPF} = 3$ there are 3 predicted cut-on modes; two corresponding to an azimuthal order of $m = -6$ and one with an azimuthal order of $m = 18$. From the far-field model calibration the dominant mode is expected to be of order 18 and the sensor spacing was therefore reduced to 3.6° to provide adequate resolution.

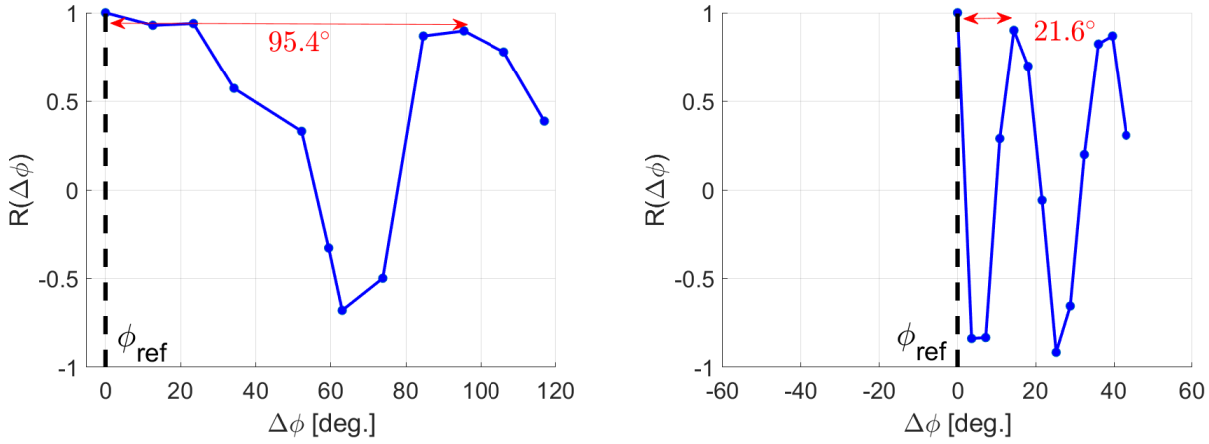

Figure 5.1: Near-field azimuthal correlations.(a) $n_{BPF} = 2$; (b) $n_{BPF} = 3$. The vertical dashed line indicates the position of the reference sensor.

The near-field measurements are consistent with the azimuthal order of the dominant mode with a peak correlation spacing of 21.6°.

While some discrepancies exist between the predicted azimuthal orders and the experimental measurements (more significantly with the 2^{nd} harmonic) the general azimuthal distribution is consistent between the two. For the remainder of the analysis, the work will assume that the pressure field follows the theoretical pressure distributions with the notion that this provides a valid approximation for the true azimuthal distributions provided in this section.

5.2 Partial Field Reconstruction

A reconstruction of the axial pressure distribution is investigated next. The pressure is obtained from the raw sensor signals using PFD as outlined in section 3.4. The experiment setup used for PFD follows the axial scanning procedure outlined in section 4.3 and spectral estimation follows the guidelines presented in section 3.3. The harmonic signal is extracted from the CSD by selecting the peak value in the region surrounding the frequency of the harmonic.

As discussed in section 3.4, accurate calculation of the CSM requires sufficient separation in the singular values of the reference CSM. The separation between singular values depends on the reference sensor location as well as the total number of reference sensors used. Figure 5.2 plots the singular values of the reference CSM when all available reference sensors are used whereas, Fig. 5.3 shows the singular values resulting from using only the two references microphones closest to the scan line. One can see that the 2^{nd} harmonic is almost completely captured by the leading partial field and is rather insensitive to the choice of reference sensors. Conversely, the 3^{rd} harmonic appears to be extremely sensitive to the reference sensors used, showing more tone energy being captured by the leading partial field when less reference sensors are used. This is possibly due to the drastic differences in the azimuthal nature of the tones however, the cause cannot be diagnosed at this point. While the separation between partial fields for the 3^{rd} harmonic is not as significant as the 2^{nd} harmonic, reasonable results could still be obtained using the two reference sensors closest to the scan line as reference. For the analysis only the leading partial field is used for determining the pressure distribution. A sample count of $J = 2048$ was used for spectral estimation of $n_{BPF} = 2$ while $J = 1024$ was used for $n_{BPF} = 3$.

The partial fields obtained from Eq. (3.15) are crucial for constructing the CSM used in characterization of the tonal components. Figure 5.4 shows the decomposed amplitude and unwrapped phase for the 2^{nd} and 3^{rd} harmonic in their raw form and after reconstruction following the procedure in section 4.4. The reconstruction shows satisfactory smoothing and interpolation across the measurement gap at $x/D_e = 0.55$. The reconstructed phase and amplitude are then used to reconstruct the partial fields using Eq. (4.1). The real and imaginary component of the reconstructed partial fields are provided in Fig. 5.5 in conjunction to their raw form. The resulting partial fields have a realistic distribution across the measurement gap and are now amenable to further analysis.

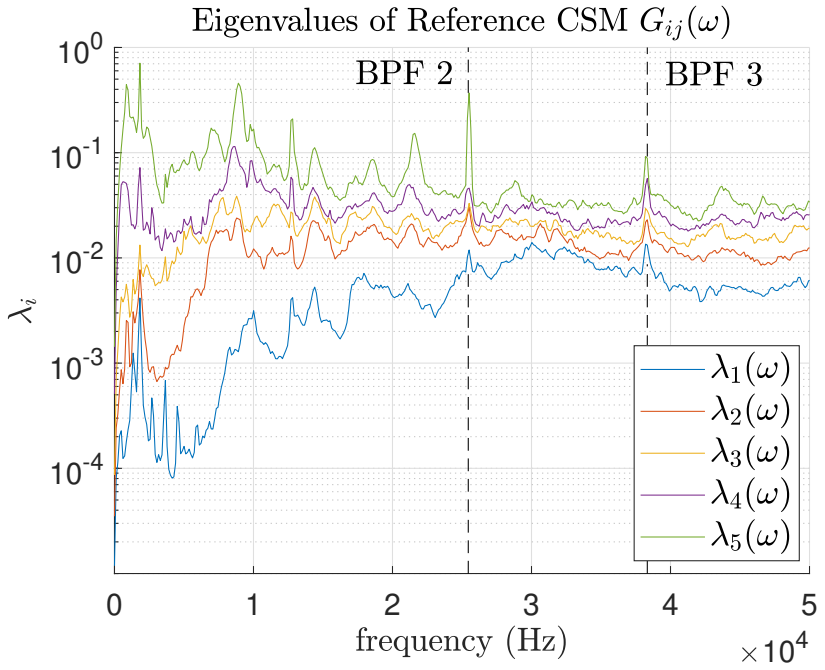

Figure 5.2: Ranked singular values of partial field decomposition for $n_{BPF} = 2$. The vertical dashed line indicates the frequency of each harmonic.

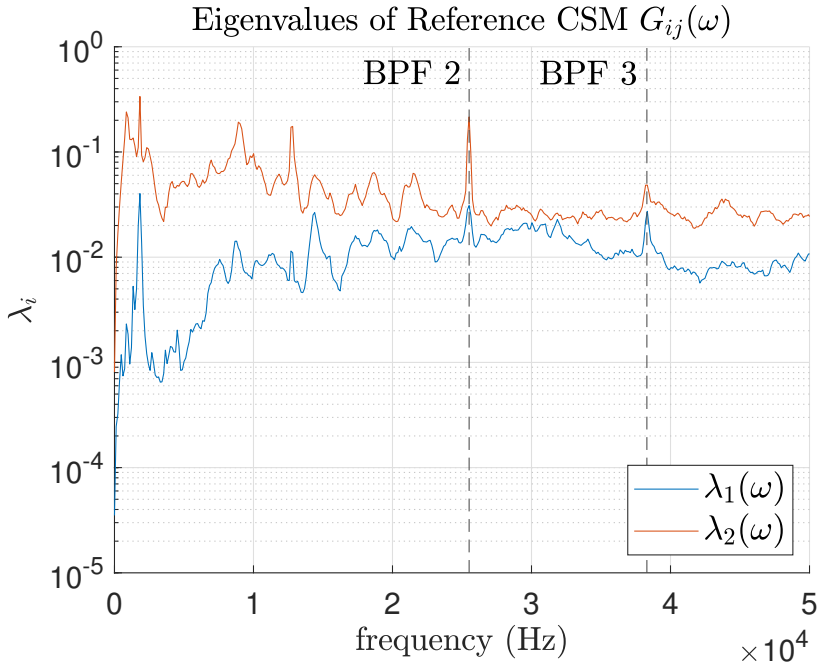

Figure 5.3: Ranked singular values of partial field decomposition for $n_{BPF} = 3$. The vertical dashed line indicates the frequency of each harmonic.

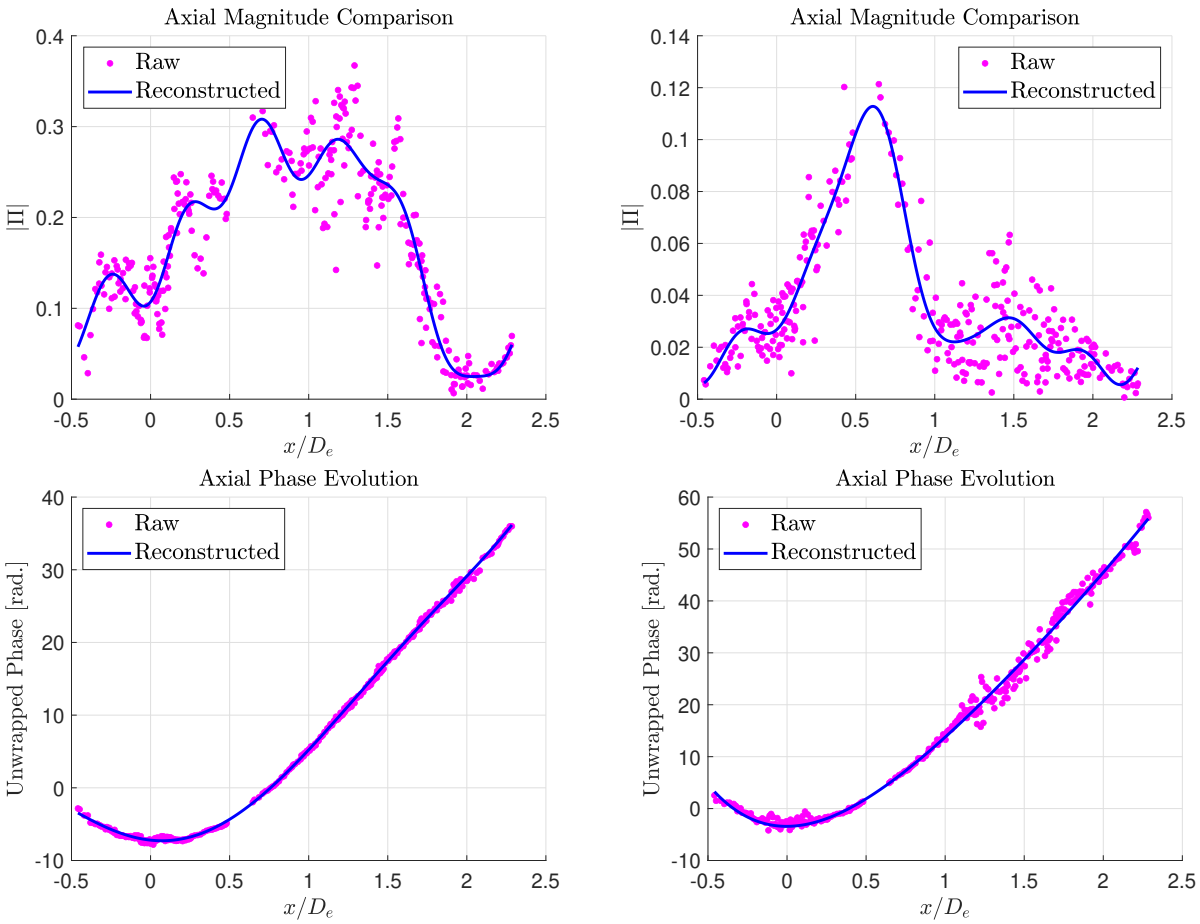

Figure 5.4: Axial distributions along scan line of the components of the leading partial field. Left column: $n_{BPF} = 2$; right column: $n_{BPF} = 3$. Top row: amplitude; bottom row: unwrapped phase. Symbols indicate raw distributions and solid lines depict their reconstructions.

The waveforms prescribed by the model described in section 2.4 are propagated from the source surface, $r/D_e = 0.5$, to the scan line of the experiments using Eq. (2.32). As with the partial fields, the modeled pressure is decomposed into its amplitude and unwrapped phase. The modeled pressure distribution on the scan line is plotted in Fig. 5.6 along with the reconstructed partial fields. The modeled unwrapped phase is in good agreement with the unwrapped phase of the partial fields for both $n_{BPF} = 2$ and 3. Concerning the amplitude, for $n_{BPF} = 2$ the modeled distribution is shifted downstream compared to the experimental one and does not decay as rapidly. For $n_{BPF} = 3$, the modeled and experimental amplitude distributions are generally in good agreement. The complete partial fields reflect the above trends, i.e., a discrepancy in amplitude for $n_{BPF} = 2$ and a fairly good match for $n_{BPF} = 3$.

For each harmonic, the partial fields are modulated azimuthally using Eq. (3.18) to form a radiation boundary condition on a cylindrical surface. The surface can be used with linear propagation methods to predict far-field emissions and include diffraction from airframe surface. The real component of the pressure on the radiator surface is presented in Fig. 5.7. The modeled and experimental pressure fields are in reasonable agreement with the discrepancies corresponding to the differences seen in Fig. 5.6.

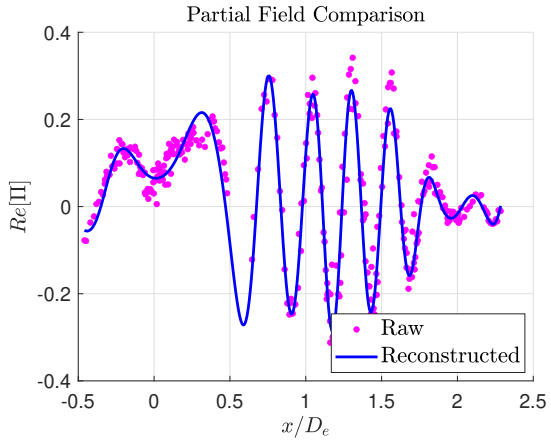

(a) Real BPF 2

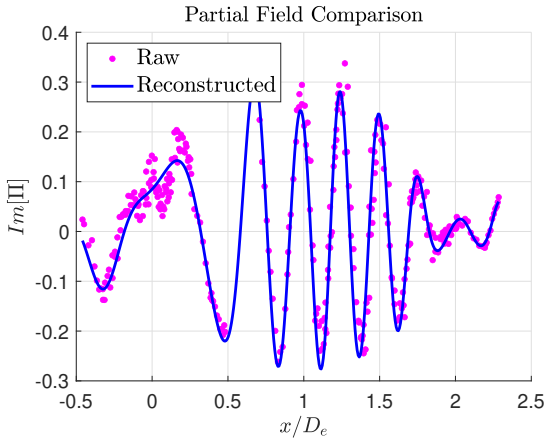

(b) Imag BPF 2

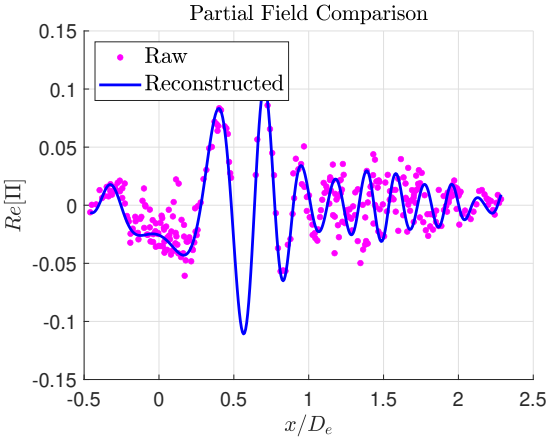

(c) Real BPF3

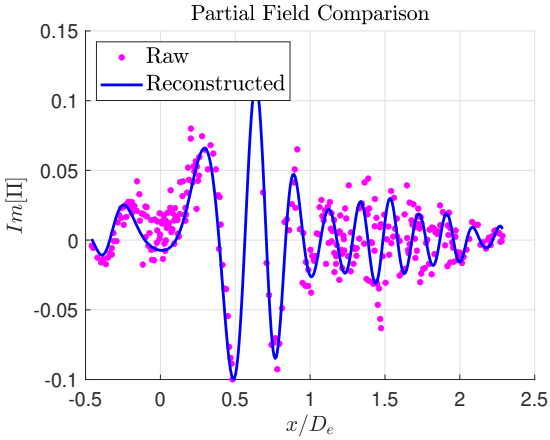

(d) BPF 3

Figure 5.5: Axial distributions along scan line of the leading partial field. Left column: real component; right column: imaginary component. Top row: $n_{BPF} = 2$; bottom row: $n_{BPF} = 3$. Symbols indicate raw distributions and solid lines depict their reconstructions.

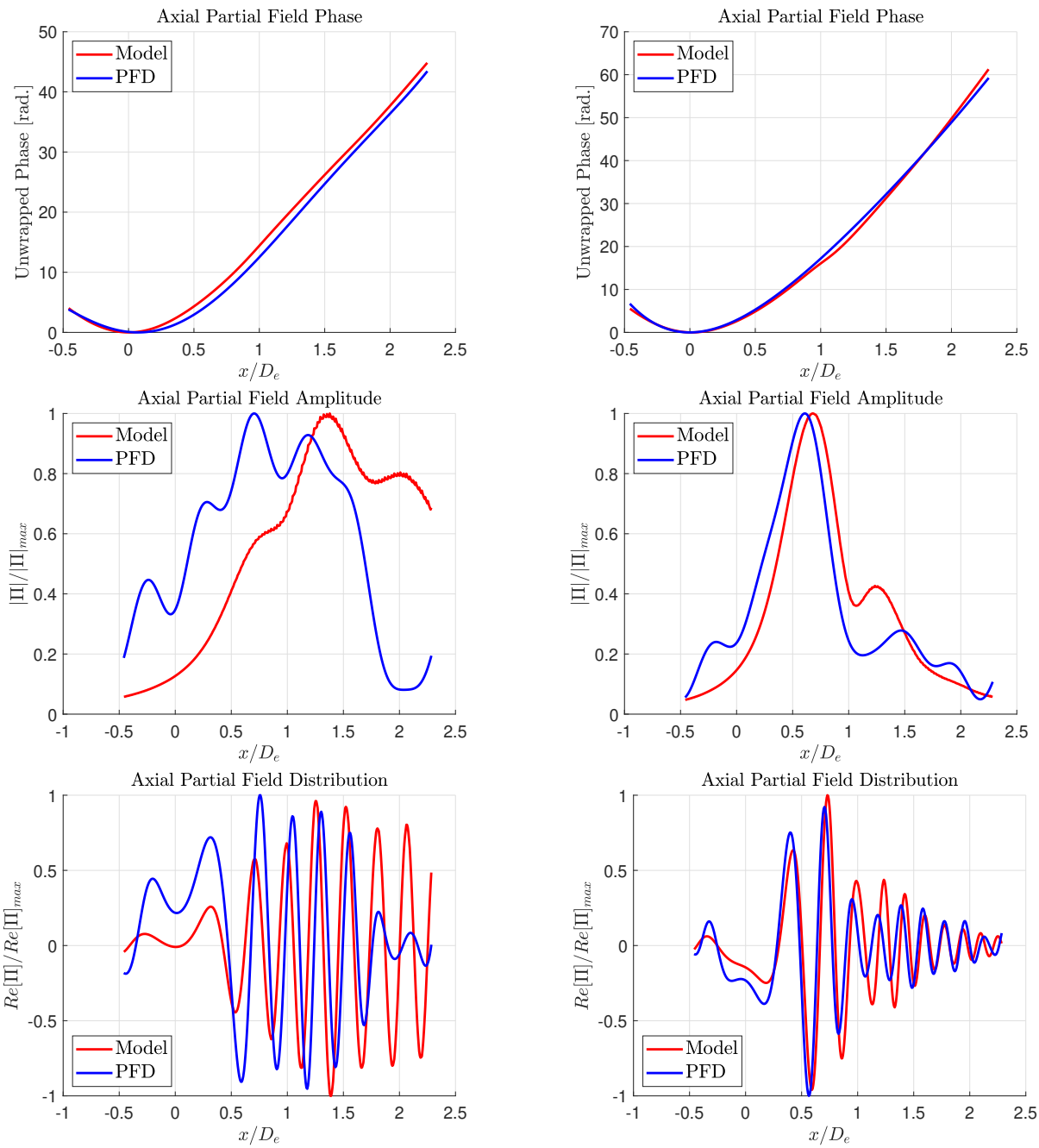

Figure 5.6: Axial distributions along scan line of modeled (red lines) and experimental (blue lines) pressures, the latter based on the reconstructed partial fields. Left column: $n_{BPF} = 2$; right column: $n_{BPF} = 3$. Top row: unwrapped phase; middle row: amplitude; bottom row: real part of pressure.

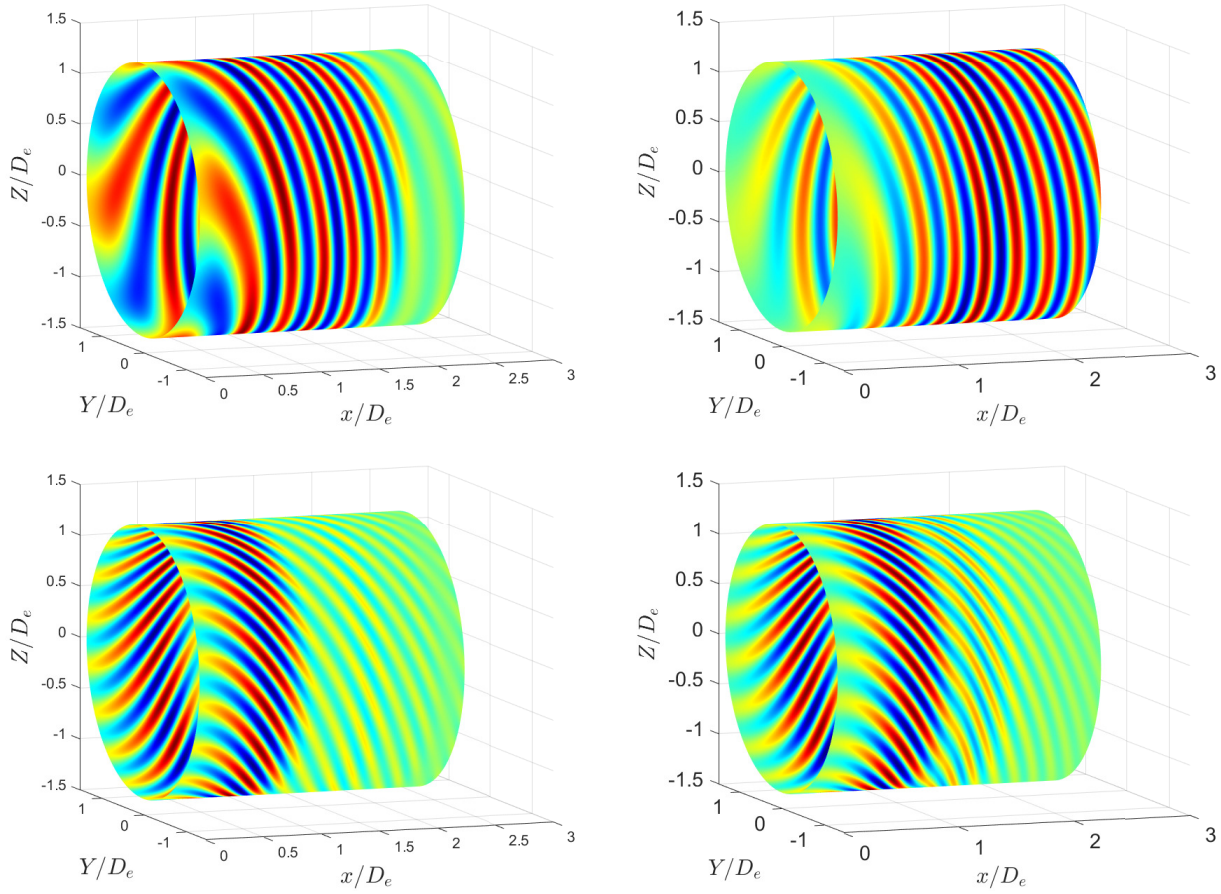

Figure 5.7: Pressure distributions on a cylindrical radiator surface. Left column: measured; right column: modeled. Top row: $n_{BPF} = 2$; bottom row: $n_{BPF} = 3$.

5.3 Axial Correlation Field

The source model is parameterized by the far-field cross-spectral densities however, it is of interest to determine if the far-field formulation can provide accurate predictions for the correlations in the near-field. The axial correlations were preformed on the scan line $r/D_e = 1.34$ and $\phi = -90°$ using Eq. (3.6). The reference sensor was placed at $x_{ref}/D_e = 0.55$. Three types of pressures were used: the measured pressure after VK filtering; the pressure of the reconstructed partial field; and the modeled pressure.

The correlations resulting from the VK-filtered pressure underwent the reconstruction procedures of section 4.4. Figure 5.8 plots the correlations for $n_{BPF} = 2$ and $n_{BPF} = 3$ in their raw form and after reconstruction. The amplitude reconstruction for $n_{BPF} = 3$ is troublesome due to the sporadic values of the raw measurement however, the resulting reconstruction still produces satisfactory smoothing and interpolation across the measurement gap at $x/D_e = 0.55$.

Figure 5.9 plots isocontours of $R(x/D_e, \tau a/D_e)$ for the aforementioned pressures for $n_{BPF} = 2$ and 3. The correlations are presented in the normalized coordinates $x/D_e = (x_{ref} + \xi)/D_e$ and $\tau a/D_e$. The correlations obtained using the VK-filtered signal are very close to the correlations obtained from the partial fields and in general are in good agreement with the model predictions. For axial locations close to the reference sensor, the slope of the isocorrelation line $R(x/D_e, \tau a/D_e)$ =const. is inversely proportional to the convective Mach number M_c. A slope of 1 indicates waves propagating from left to right with the speed of sound. For all cases the contour slope is near zero around $x = 0$, indicating wavefronts that are traveling laterally with respect to the fan axis and whose trace along the scan line propagates at near-infinite speeds. The propagation speed declines with downstream distance, reaching near sonic speed at far downstream locations.

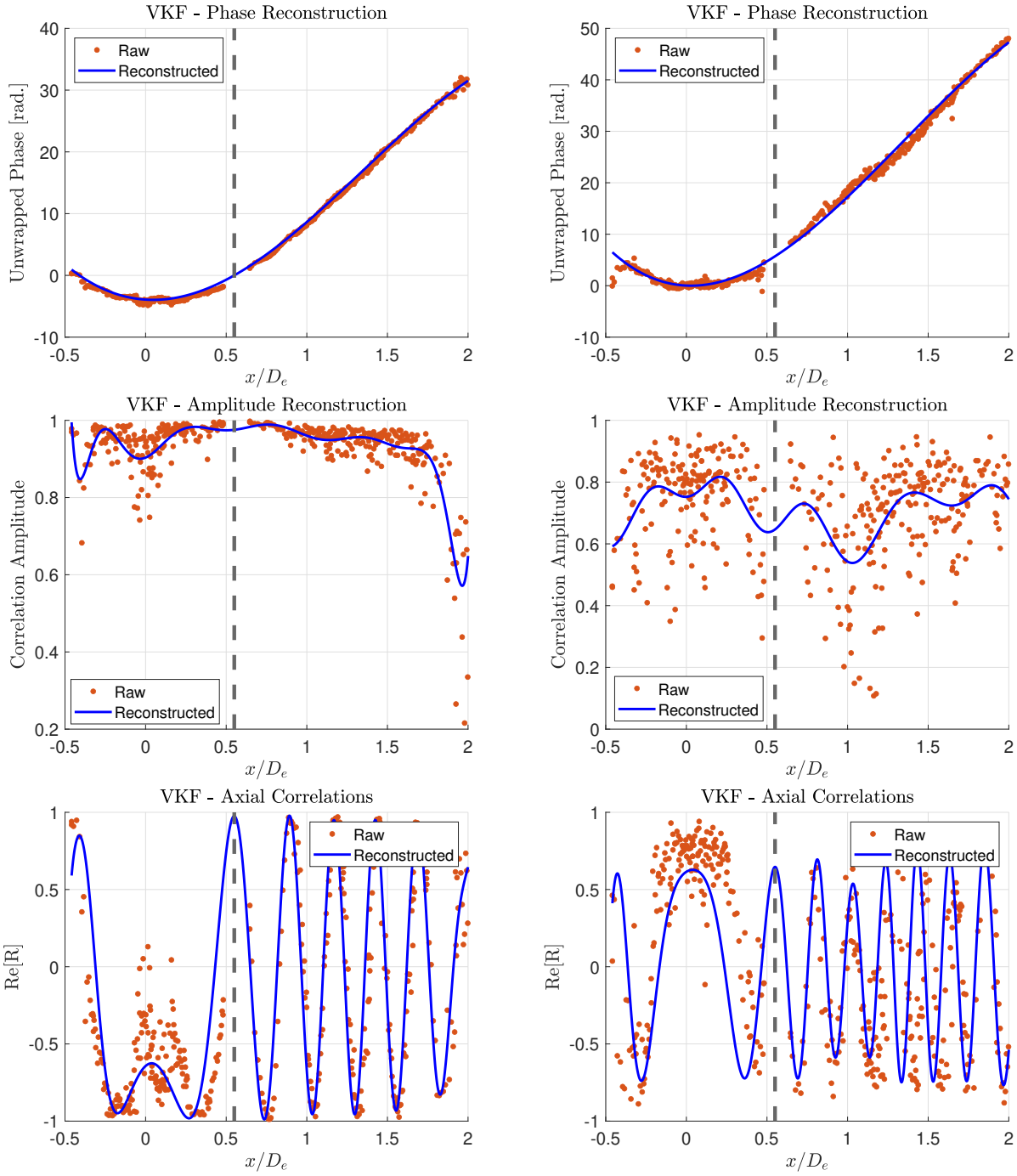

Figure 5.8: Axial distributions along scan line of correlations obtained using the VK-filtered pressure field for left column: $n_{BPF} = 2$; right column: $n_{BPF} = 3$. Top row: unwrapped phase; middle row: amplitude; bottom row: real component of correlation

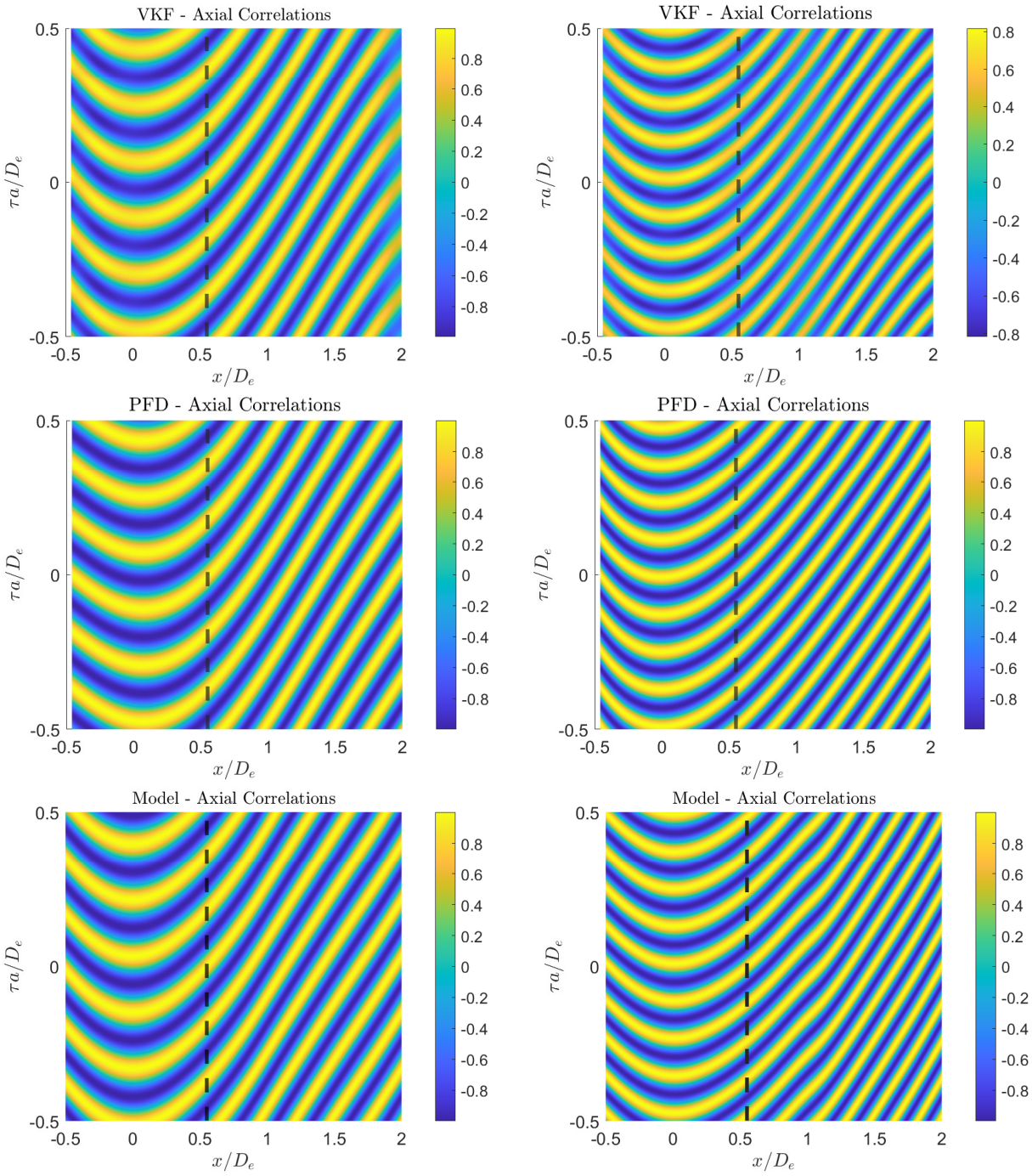

Figure 5.9: Isocontours of space-time correlations on the scan line with reference sensor at $x_{ref}/D_e = 0.55$ (vertical dashed lines). Left column: $n_{BPF} = 2$; right column: $n_{BPF} = 3$. Top row: VK-filtered signal; middle row: reconstructed partial field; bottom row: model.

5.4 Convective Mach Number

The qualitative agreement of the modeled and experimental axial correlations seen in Fig. 5.9 motivated a quantitative assessment of the convective velocity. Recalling that the convective velocity is inversely proportional to the iso-correlation lines, this can be expressed as

$$dR(x;\xi,\tau) = 0 \tag{5.1}$$

Expansion around a reference position x yields

$$\frac{\partial R}{\partial \xi} d\xi + \frac{\partial R}{\partial \tau} d\tau = 0 \tag{5.2}$$

The convective velocity is related to the iso-correlation slope around x by

$$U_c(x) = \frac{d\xi}{d\tau} = -\frac{\partial R/\partial \tau}{\partial R/\partial \xi} \tag{5.3}$$

For a harmonic signal, the correlation is given by Eq.3.3. Letting $Q(x;\xi) = P(x)P^*(x+\xi)$ the convective velocity is then given by

$$U_c(x) = -\frac{i\omega Q(x;0)}{[\partial Q(x;\xi)/\partial \xi]_{\xi=0}} \tag{5.4}$$

The convective Mach number is then given by $M_c = U_c/a$ where a is the ambient speed of sound.

An important attribute of the PFD in conjunction with the continuous-scan paradigm is that each partial field is finely resolved enough to allow computation of $U_c(x)$ throughout the entire scan line. A potential difficulty in using the VK-filtered signal however, is that the space time correlations can only be obtained between scanning sensors of the same block or between the scanning sensors and the fixed (reference) sensor located at x_{ref}. In the

former case, the spatial separation ξ is too coarse to accurately determine $U_c(x)$; in the latter scenario, only $U_c(x_{ref})$ can be determined. To circumnavigate these issues the signals resulting from the VK-filter were expressed as

$$p(x,t) = e^{if(x)}e^{-i\omega t} \tag{5.5}$$

The correlation between the reference sensor and a sensor at a location $x_{ref} + \xi_1$ is then given as

$$R(x;\xi_1) = exp\left[i(f(x) - f(x+\xi_1))\right] e^{i\omega\tau} \tag{5.6}$$

Similarly, the correlation between the reference sensor and a sensor at a location $x_{ref} + \xi_2$ is given by

$$R(x;\xi_2) = exp\left[i(f(x) - f(x+\xi_2))\right] e^{i\omega\tau} \tag{5.7}$$

For two closely spaced points, one can then theoretically compute the correlation between two independent measurements as

$$R(x+\xi_1;\xi_2-\xi_1) = \frac{R(x;\xi_2)}{R(x;\xi_1)} \tag{5.8}$$

The correlation given by Eq. (5.8) can then be used to calculate the convective velocity $U_c(x+\xi_1)$ from Eq. (5.4).

The convective Mach number distributions evaluated using the leading partial field and the VK-filtered signal are presented in Figs. 5.10 and 5.11 along with the distribution predicted by the model. For the majority of the domain, the convective Mach number obtained from the VK-filtered signal and the partial fields are very close and the overall trends between model and experiment are consistent. The convective Mach number predictions show near-

infinite M_c near $x = 0$ (indicating lateral propagation of acoustic waves) and negative M_c for $x < 0$ (upstream propagation). The convective Mach number obtained using PFD and the model prediction shows rapidly declining, positive M_c for $x > 0$ whereas, the convective Mach number computed from the VK-filtered signal shows an acceleration in M_c for $x > 1.5$. The origin of this discrepancy was not investigated during this study. For $n_{BPF} = 2$, the model over predicts the rate of decline for $x/D_e < 0.5$ but matches well the experiment downstream obtained from PFD. The model predictions and distribution resulting from PFD reach $M_c \approx 1.2$ at $x/D_e = 2$. For $n_{BPF} = 3$ the modeled distribution is in very close agreement to the distribution resulting from PFD throughout the surveyed region. Recalling that the model was calibrated based on far-field acoustic data, the agreement seen in Figs. 5.10 and 5.11 provides encouragement that the model captures the fundamental physics of noise emission.

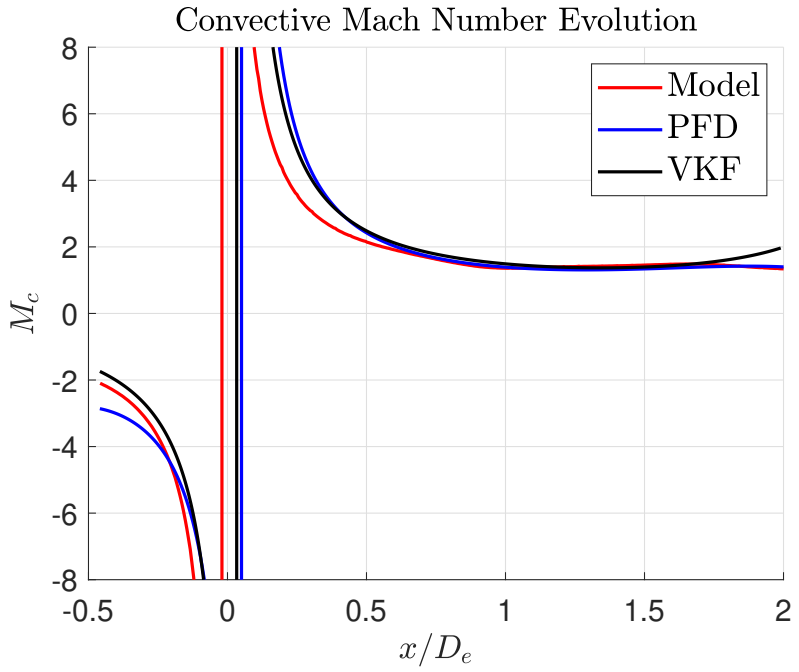

Figure 5.10: Axial distribution of the convective Mach number on the scan line based on the correlations obtained from PFD (blue line) VK filtering (black line) and model predictions (red line) for $n_{BPF} = 2$.

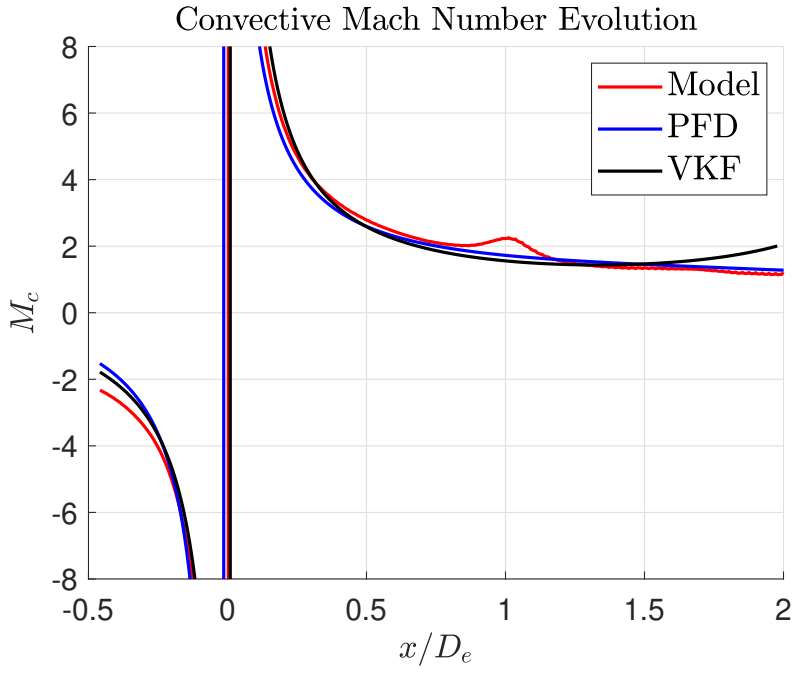

Figure 5.11: Axial distribution of the convective Mach number on the scan line based on the correlations obtained from PFD (blue line) VK filtering (black line) and model predictions (red line) for $n_{BPF} = 3$.

5.5 Sound Pressure Level

Far-field measurements suggest that each tonal component has a region of peak emission corresponding to a polar angle reminiscent of Mach wave radiation [18]. For measurements in the near-field however, this assumption may no longer be valid. The axial SPL is therefore studied to determine the accuracy of the near-field directivity predicted by the model.

The raw SPL is calculated using Eq. (2.6) with the pressures obtained from PFD and the model predictions. Figure 5.12 shows the resulting axial SPL for $n_{BPF} = 2$ and 3. The SPL distribution for both tones is highly directive and is more significant for $n_{BPF} = 3$. The SPL for $n_{BPF} = 2$ peaks between $0.5 \leq x/D_e \leq 1.5$ before drastically decreasing for $x/D_e \geq 1.5$. For $n_{BPF} = 3$ there are two regions of peak emission occurring at approximately $x/D_e = 0.55$ and $x/D_e = 1.5$.

For $n_{BPF} = 2$ duct acoustics predicts two cut-on modes with a corresponding emission angle of 49.2 and 67.8 degrees. For the given experiment parameters, this corresponds to the axial coordinates of $x = 1.15D_e$ and $x = 0.55D_e$. The region of predicted peak emission is somewhat consistent with the measured SPL distribution however, the model drastically under predicts the SPL for $x/D_e \leq 1$ suggesting that the modeled mode contributions may need refinement. It is also possible for far upstream locations, that the experimental SPL faces issues such as scanning the acoustic field too rapidly or experiencing contamination from inlet noise.

For $n_{BPF} = 3$ there are 3 predicted cut-on modes with a peak emission angle of 49.2°, 57.4° and 69.5°. This corresponds to axial locations $x/D_e = 1.15$, 0.86 and 0.50 respectively. The measured axial SPL for BPF 3 is consistent with the most upstream emission angle however deviates from theoretical values for the remaining modes. This may suggest that the assumption of emission direction based on Mach wave radiation is not applicable in the near-field.

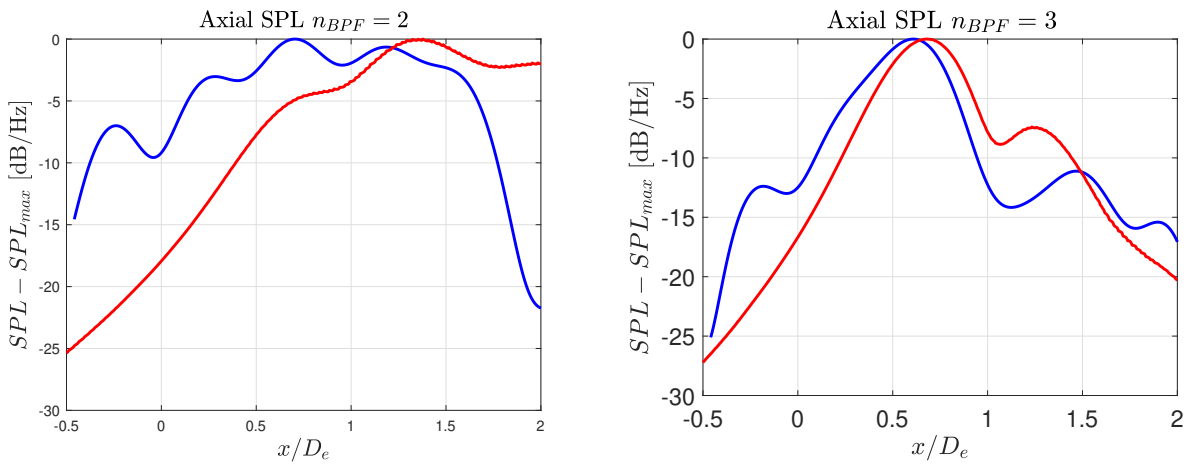

Figure 5.12: Axial sound pressure level distribution based on pressure obtained using PFD (blue line) and predicted by model (red line) for left: $n_{BPF} = 2$; right: $n_{BPF} = 3$.

While their appears to be some correlation between the predicted peak emission angles resulting from Mach wave radiation, the measurements are currently insufficient to confirm this assumption in the near-field. During the investigation, the tonal pressure field was also found to be highly dependent on the operational RPM which inevitably shifted from one experiment to the next.

Chapter 6

Conclusion

6.1 Summary

The purpose of this work was to utilize advanced experimental setups consisting of fixed and scanning sensors and apply it to high-resolution imaging of aeroacoustic sources. The sensor array included a stationary azimuthal ring in conjunction with a linear array that scanned the axial coordinate. The use of scanning sensors requires special techniques for spectral estimation and requires that the signal is divided into quasi-stationary blocks to account for non-stationarity in the acoustic field. Spectral estimation and block division followed the guidelines proposed by Papamoschou and Morata [27].

Two distinct methodologies for the processing of harmonic noise sources using continuously-scanning sensors was presented. The first is a time domain analysis that utilized an order tracking signal to extract the harmonic contributions from the acoustic spectrum. The extracted harmonic components were then used with the space-time correlation to reconstruct the acoustic field. The main drawback to this approach is the need for an accurate tracking signal to properly isolate the tone contributions. The second technique, PFD, was used pre-

viously for near-field acoustic holography and has recently gained interest within the context of continuously-scanning arrays. PFD is capable of producing noise maps with high spatial resolution equivalent to what was obtained through the VK filter however, with the added benefit of requiring no reference vector.

Both methodologies investigated were used to produce high-resolution imaging of the acoustic near-field. The resulting acoustic images was used to verify a surface-based source model, proposed by Papamoschou [1], that was parameterized by far-field measurements. The axial correlations for both methods were constructed through interpolation of the phase and amplitude decomposition which yielded far superior results to traditional filtering and interpolation techniques. Azimuthal measurements suggest that the azimuthal order of each Tyler-Sofrin mode is retained outside of the duct however, may be subject to disturbances by the duct geometry. The azimuthal measurements were combined with the scanning axial measurements to allow for the construction of a cylindrical radiating surface using PFD. The resulting surface showed good agreement to the model predictions. Additionally, linearization of the axial correlations allowed for the calculation of the convective Mach number and was used to verify the decay function used in the surface based model. While both methods showed reasonable agreement to the model parameterization, PFD seems to more accurately capture the convective Mach number at far downstream positions.

6.2 Future Work

Continuation of this work arises in the refinement of both the aft-emission model parameterization and the experimental procedure. While the phase decomposition and convective Mach number were accurately predicted by the model, the axial pressure amplitude contained discrepancies, more evidently for $n_{BPF} = 2$. Further investigation is required to determine if this discrepancy is a result of the model parameterization or if it originates from insufficient

experimental procedures such as the sensor scan speed. Additional experiments can be performed utilizing various scan speeds with the ultimate goal being to properly capture the acoustic field.

A natural extension of this work includes application of the measured acoustic field to already developed propagation tools. The pressure surfaces generated through PFD and the model can be implemented into propagation prediction tools such as, BEM [29] to predict the acoustic far-field at spatial locations where current measurements are available. The measured and predictive far-fields can then be compared for reference.

Inspired by the promising results of this work, future goals include attempting to generate surface base models for other noise sources. The next step for modeling of turbofan engine noise would include applying this procedure to the modeling of tonal inlet fan noise. Modeling of inlet noise through source surfaces will require far-field measurements through which it can be parameterized and validated against near-field measurements.

A topic of further exploration includes the optimization of reference sensor placement for use in PFD. While some comparison in reference sensor placement was explored in this work, a optimal and systematic procedure for reference sensor placement is required to enhance the applicability of PFD to the characterization of aeroacoustic sources.

Lastly, as seen by the correlation reconstructions using the VK filter, the use of a singular reference sensor along the scan line may be insufficient. This work utilized a theoretical approach to correlating two independent measurements however this procedure should be further explored to determine its validity.

Bibliography

[1] D. Papamoschou. Modeling of aft-emitted tonal fan noise in isolated and installed configurations. *AIAA Paper 2021-0009*, 2021. doi: 10.2514/6.2021-0009.

[2] HISTORYNET STAFF. St. petersburg tampa airboat line: World's first scheduled airline using winged aircraft, 2006. URL `https://www.historynet.com`. Accessed: 2023-05-30.

[3] Icao - future of aviation. URL `https://www.icao.int/Pages/default.aspx`. Accessed: 2023-05-30.

[4] T. Elliff and Huck-V. Cremaschi, M. Impact of aircraft noise pollution on residents of large cities. *Policy Department for Citizens' Rights and Constitutional Affairs*, 2020. doi: PE650.787.

[5] D. Morata. High-resolution localization of aeroacoustic sources using advanced phased array setups. *Ph.D Thesis, University of California, Irvine*, 2022.

[6] U. Michel. History of acoustic beamforming. *Berlin Beamforming Conference*, 2006.

[7] Hicks C. and H. Hubbard. Comparison of sound emission from two-blade, four-blade and seven-blade propellers. *NACA TN 1354*, 1947.

[8] H. Hubbard and A. Regier. Propeller-loudness charts for light airplanes. *NACA TN 1358*, 1947.

[9] H. Hubbard. Sound measurements for five shrouded propellers at static conditions. *NACA TN 2024*, 1950.

[10] J. Tyler and T. Sofrin. Axial flow compressor noise studies. *SAE Transactions*, 70: 309–332, 1962. doi: 10.4271/620532.

[11] Heidmann-M. Rice, E. and T. Sofrin. Modal propagation angles in a cylindrical duct with flow and their relation to sound radiation. 1979.

[12] R.M. Munt. The interaction of sound with a subsonic jet issuing from a semi-infinite cylindrical pipe. *J. Fluid Mech.*, 83:609–640, 1977.

[13] Harper-Bourne M. Fisher, M.J. and S.A.L. Glegg. Jet engine noise source location: The polar correlation technique. *Journal of Sound and Vibration*, pages 23–54, 1977.

[14] Zhang-X. Chen X. Richards, S. and P.A. Nelson. Evaluation of non-reflecting boundary conditions for duct acoustic computation. *Journal of Sound and Vibration*, 270(3): 539–557, 2004. doi: 10.1016/j.jsv.2003.09.042.

[15] X. Zhang, Morfey-C.L. Chen, X., and Nelson P.A. Computation of spinning modal radiation from an unflanged duct. *AIAA Journal*, 42(9):1795–1801, 2004.

[16] X. Zhang, Morfey Chen, X., and C.L. Acoustic radiation from a semi-infinite duct with a subsonic jet. *International Journal of Aeroacoustics*, 4(1-2):169–184, 2005.

[17] Chen-X. Huang X. Richards, S. and X. Zhang. Computation of fan noise radiation through an engine exhaust geometry with flow. *International Journal of Aeroacoustics*, 6(3):223–241, 2007.

[18] Chen-Z. Ma Z. Huang, X. and X. Zhang. Efficient computation of spinning modal radiation through an engine bypass duct. *AIAA Journal*, 50:1029–1046, 2012. doi: 10.2514/1.J050730.

[19] M. Lee and Bolton S. Source characterization of a subsonic jet by using near-field acoustical holography. *The Journal of the Acoustical Society of America*, 121(2):967–977, 2007.

[20] Vold-H. Hensley D. Envia E. Shah, P. and D. Stephens. A High-Resolution Continuous-Scan Acoustic Measurement Method for Turbofan Engine Applications. *Journal of Turbomachinery*, 137(12), 09 2015. ISSN 0889-504X. doi: 10.1115/1.4031341. URL `https://doi.org/10.1115/1.4031341`. 121002.

[21] Miller-K. Morata, D. and D. Papamoschou. Experimental study of underexpanded screeching jet and its interaction with upstream reflector. *AIAA paper 2022-2868*. doi: 10.2514/6.2022-2868.

[22] R. Liebeck. Design of the blended wing body subsonic transport. *Journal of Aircraft*, 41:10–25, 2004. doi: 10.2514\1.9084.

[23] A. Truong. Experimental and theoretical investigation of the emission and diffraction of discrete tone noise generated from the exhaust of a ducted fan. *Ph.D Thesis, University of California, Irvine*, 2018.

[24] D Papamoschou. Improved modeling of aft-emitted tonal noise from a ducted fan. *Abstract submitted to AIAA Aviation 2023*, 2023.

[25] D. Papamoschou. Prediction of jet noise shielding. *AIAA Paper 2010-0653*, 2010. doi: 10.2514/6.2010-653.

[26] D. Papamoschou. Wavepacket modeling of the jet noise source. *Journal of Sound and Vibration*, 330:2265–2280, 2018. doi: 10.1016/j.jsv.2010.11.025.

[27] Morata-D. Papamoschou, D. Inverse acoustic methodology for continuous-scan phased arrays. *AIAA Journal*, 57, 2019. doi: 10.2514/1.J058085.

[28] M. Debiasi. Acoustics of dual-stream high-speed jets. *PhD thesis, University of California, Irvine*, 2000.

[29] Y.J. Liu. Fast multipole boundary element method - theory and application in engineering. 2009.

[30] H. Vold and Leuridan J. High resolution order tracking at extreme slew rates using kalman tracking filters. *SAE Technical Paper 931288*, 1993.

[31] D. Stephens and H. Vold. Order tracking signal processing for open rotor acoustics. *Journal of Sound and Vibration*, 333:3818–3830, 2014. doi: 10.1016/j.jsv.2014.04.005.

[32] A. Truong and Papamoschou D. Harmonic and broadband separation of noise from a small ducted fan. *AIAA Paper 2015-3282*, 2015. doi: 10.2514/6.2015-3282.

[33] *Continuous-Scan Phased Array Measurement Methods for Turbofan Engine Acoustic Testing*, volume 2B: Turbomachinery of *Turbo Expo: Power for Land, Sea, and Air*, 06 2018. doi: 10.1115/GT2018-77033. V02BT43A012.

[34] Vold-H. Shah, P. and M. Yang. Reconstruction of far-field noise using multi-reference acoustical holography measurements of high-speed jets. *Technical report, AIAA Paper*, 2011. doi: 10.2514/6.2011-2772.